High-Resolution Photoemission on Sr_2RuO_4 Reveals Correlation-Enhanced Effective Spin-Orbit Coupling and Dominantly Local Self-Energies

A. Tamai,[1,*] M. Zingl,[2] E. Rozbicki,[3] E. Cappelli,[1] S. Riccò,[1] A. de la Torre,[1] S. McKeown Walker,[1] F. Y. Bruno,[1] P. D. C. King,[3] W. Meevasana,[4] M. Shi,[5] M. Radović,[5] N. C. Plumb,[5] A. S. Gibbs,[3,†] A. P. Mackenzie,[6,3] C. Berthod,[1] H. U. R. Strand,[2] M. Kim,[7,8] A. Georges,[9,2,8,1] and F. Baumberger[1,5]

[1]*Department of Quantum Matter Physics, University of Geneva, 24 Quai Ernest-Ansermet, 1211 Geneva 4, Switzerland*
[2]*Center for Computational Quantum Physics, Flatiron Institute, 162 5th Avenue, New York, New York 10010, USA*
[3]*SUPA, School of Physics and Astronomy, University of St. Andrews, St. Andrews, Fife KY16 9SS, United Kingdom*
[4]*School of Physics, Suranaree University of Technology and Synchrotron Light Research Institute, Nakhon Ratchasima, 30000, Thailand and Thailand Center of Excellence in Physics, CHE, Bangkok, 10400, Thailand*
[5]*Swiss Light Source, Paul Scherrer Institut, CH-5232 Villigen PSI, Switzerland*
[6]*Max Planck Institute for Chemical Physics of Solids, D-01187 Dresden, Germany*
[7]*Department of Physics and Astronomy, Rutgers, The State University of New Jersey, Piscataway, New Jersey 08854, USA*
[8]*Centre de Physique Théorique, CNRS, Ecole Polytechnique, IP Paris, F-91128 Palaiseau, France*
[9]*Collège de France, 11 place Marcelin Berthelot, 75005 Paris, France*

(Received 16 December 2018; revised manuscript received 27 March 2019; published 6 June 2019)

We explore the interplay of electron-electron correlations and spin-orbit coupling in the model Fermi liquid Sr_2RuO_4 using laser-based angle-resolved photoemission spectroscopy. Our precise measurement of the Fermi surface confirms the importance of spin-orbit coupling in this material and reveals that its effective value is enhanced by a factor of about 2, due to electronic correlations. The self-energies for the β and γ sheets are found to display significant angular dependence. By taking into account the multi-orbital composition of quasiparticle states, we determine self-energies associated with each orbital component directly from the experimental data. This analysis demonstrates that the perceived angular dependence does not imply momentum-dependent many-body effects but arises from a substantial orbital mixing induced by spin-orbit coupling. A comparison to single-site dynamical mean-field theory further supports the notion of dominantly local orbital self-energies and provides strong evidence for an electronic origin of the observed nonlinear frequency dependence of the self-energies, leading to "kinks" in the quasiparticle dispersion of Sr_2RuO_4.

DOI: 10.1103/PhysRevX.9.021048

Subject Areas: Condensed Matter Physics, Strongly Correlated Materials

I. INTRODUCTION

The layered perovskite Sr_2RuO_4 is an important model system for correlated electron physics. Its intriguing superconducting ground state, sharing similarities with superfluid ^{3}He [1–3], has attracted much interest and continues to stimulate advances in unconventional superconductivity [4]. Experimental evidence suggests odd-parity spin-triplet pairing, yet questions regarding the proximity of other order parameters, the nature of the pairing mechanism, and the apparent absence of the predicted edge currents remain open [3–9]. Meanwhile, the normal state of Sr_2RuO_4 attracts interest as one of the cleanest oxide Fermi liquids [10–13]. Its precise experimental characterization is equally important for understanding the unconventional superconducting ground state of Sr_2RuO_4 [1–9,14–17], as it is for benchmarking quantitative many-body calculations [18–23].

*Corresponding author.
anna.tamai@unige.ch
†Present address: ISIS Facility, Rutherford Appleton Laboratory, Chilton, Didcot OX11 OQX, United Kingdom.

Published by the American Physical Society under the terms of the Creative Commons Attribution 4.0 International license. Further distribution of this work must maintain attribution to the author(s) and the published article's title, journal citation, and DOI.

Transport, thermodynamic, and optical data of Sr_2RuO_4 display textbook Fermi-liquid behavior below a crossover temperature of $T_{FL} \approx 25$ K [10–13]. Quantum oscillation and angle-resolved photoemission spectroscopy (ARPES) measurements [24–34] further reported a strong enhancement of the quasiparticle effective mass over the bare band mass. Theoretical progress has been made recently in revealing the important role of the intra-atomic Hund's coupling as a key source of correlation effects in Sr_2RuO_4 [18,20,35]. In this context, much attention was devoted to the intriguing properties of the unusual state above T_{FL}, which displays metallic transport with no signs of resistivity saturation at the Mott-Ioffe-Regel limit [36]. Dynamical mean-field theory (DMFT) [37] calculations have proven successful in explaining several properties of this intriguing metallic state, as well as in elucidating the crossover from this unusual metallic state into the Fermi-liquid regime [13,18,20–23,38]. Within DMFT, the self-energies associated with each orbital component are assumed to be local. On the other hand, the low-temperature Fermi-liquid state is known to display strong magnetic fluctuations at specific wave vectors, as revealed, e.g., by neutron scattering [39,40] and nuclear magnetic resonance (NMR) spectroscopy [41,42]. These magnetic fluctuations were proposed early on to be an important source of correlations [2,43,44]. In this picture, it is natural to expect strong momentum dependence of the self-energy associated with these spin fluctuations. Interestingly, a similar debate was raised long ago in the context of liquid ^{3}He, with "paramagnon" theories emphasizing ferromagnetic spin fluctuations and "quasilocalized" approaches *à la* Anderson-Brinkman emphasizing local correlations associated with the strong repulsive hard core, leading to increasing Mott-like localization as the liquid is brought closer to solidification (for a review, see Ref. [45]).

In this work, we report on new insights into the nature of the Fermi-liquid state of Sr_2RuO_4. Analyzing a comprehensive set of laser-based ARPES data with improved resolution and cleanliness, we reveal a strong angular (i.e., momentum) dependence of the self-energies associated with the quasiparticle bands. We demonstrate that this angular dependence originates in the variation of the orbital content of quasiparticle states as a function of angle, and it can be understood quantitatively. Introducing a new framework for the analysis of ARPES data for multi-orbital systems, we extract the electronic self-energies associated with the three Ruthenium t_{2g} orbitals with minimal theoretical input. We find that these orbital self-energies have strong frequency dependence but surprisingly weak angular (i.e., momentum) dependence, and they can thus be considered local to a very good approximation. Our results provide a direct experimental demonstration that the dominant effects of correlations in Sr_2RuO_4 are weakly momentum dependent and can be understood from a local perspective, provided they are considered in relation to orbital degrees of freedom. One of the novel aspects of our work is to directly put the locality ansatz underlying DMFT to the experimental test. We also perform a direct comparison between DMFT calculations and our ARPES data, and we find good agreement with the measured quasiparticle dispersions and angular dependence of the effective masses.

The experimentally determined real part of the self-energy displays strong deviations from the low-energy Fermi-liquid behavior $\Sigma'(\omega) \sim \omega(1 - 1/Z) + \cdots$ for binding energies $|\omega|$ larger than about 20 meV. These deviations are reproduced by our DMFT calculations, suggesting that the cause of these nonlinearities are local electronic correlations. Our results thus call for a revision of earlier reports of strong electron-lattice coupling in Sr_2RuO_4 [29–31,46–50]. We finally quantify the effective spin-orbit coupling (SOC) strength and confirm its enhancement due to correlations predicted theoretically [21,23,51].

This article is organized as follows. In Sec. II, we briefly present the experimental method and report our main ARPES results for the Fermi surface and quasiparticle dispersions. In Sec. III, we introduce the theoretical framework on which our data analysis is based. In Sec. IV, we use our precise determination of the Fermi surface to reveal the correlation-induced enhancement of the effective SOC. In Sec. V, we proceed with a direct determination of the self-energies from the ARPES data. Section VI presents the DMFT calculations in comparison to experiments. Finally, our results are critically discussed and put into perspective in Secs. VII and VIII.

II. EXPERIMENTAL RESULTS

A. Experimental methods

The single crystals of Sr_2RuO_4 used in our experiments were grown by the floating zone technique and showed a superconducting transition temperature of $T_c = 1.45$ K. ARPES measurements were performed with a MBS electron spectrometer and a narrow-bandwidth 11-eV (113-nm) laser source from Lumeras that was operated at a repetition rate of 50 MHz with a 30-ps pulse length of the 1024-nm pump [52]. All experiments were performed at $T \approx 5$ K using a cryogenic 6-axes sample goniometer, as described in Ref. [53]. A combined energy resolution of 3 meV was determined from the width of the Fermi-Dirac distribution measured on a polycrystalline Au sample held at 4.2 K. The angular resolution was approximately 0.2°. In order to suppress the intensity of the surface layer states on pristine Sr_2RuO_4 [54], we exposed the cleaved surfaces to approximately 0.5 Langmuir CO at a temperature of approximately 120 K. Under these conditions, CO preferentially fills surface defects and subsequently replaces apical oxygen ions to form a Ru–COO carboxylate in which the C end of a bent CO_2 binds to Ru ions of the reconstructed surface layer [55].

B. Experimental Fermi surface and quasiparticle dispersions

In Fig. 1, we show the Fermi surface and selected constant energy surfaces in the occupied states of Sr_2RuO_4. The rapid broadening of the excitations away from the Fermi level seen in the latter is typical for ruthenates and implies strong correlation effects on the quasiparticle properties. At the Fermi surface, one can readily identify the α, β, and γ sheets that were reported earlier [25,27,28]. However, compared with previous ARPES studies, we achieve a reduced linewidth and improved suppression of the surface-layer states giving clean access to the bulk electronic structure. This is particularly evident along the Brillouin zone diagonal (ΓX), where we can clearly resolve all band splittings.

In the following, we exploit this advance to quantify the effects of SOC in Sr_2RuO_4 and to provide new insight into the renormalization of the quasiparticle excitations using minimal theoretical input only. To this end, we acquired a set of 18 high-resolution dispersion plots along radial $\boldsymbol{k}$-space lines (as parametrized by the angle θ measured from the ΓM direction). The subset of data shown in Fig. 2(a) immediately reveals a rich behavior with a marked dependence of the low-energy dispersion on the Fermi surface angle θ. Along the ΓM high-symmetry line, our data reproduce the large difference in Fermi velocity $v_F^{\beta,\gamma}$ for the β and γ sheets, which is expected from the different cyclotron masses deduced from quantum oscillations [12,25,26] and was reported in earlier ARPES studies [33,56]. Our systematic data, however, reveal that this difference gradually disappears towards the Brillouin zone diagonal ($\theta = 45°$), where all three bands disperse nearly parallel to one another. In Sec. IV, we show that this equilibration of the Fermi velocity can be attributed to the strong effects of SOC around the zone diagonal.

To quantify the angle dependence of $v_F^{\beta,\gamma}$ from experiment, we determine the maxima $\boldsymbol{k}_{\max}^{\nu}(\omega)$ of the momentum distribution curves (MDCs) over the range of 2–6 meV below the Fermi level E_F and fit these $\boldsymbol{k}$-space loci with a second-order polynomial. We then define the Fermi velocity as the derivative of this polynomial at E_F. This procedure minimizes artifacts due to the finite energy resolution of the experiment. As shown in Fig. 2(c), the Fermi velocities $v_F^{\beta,\gamma}$ obtained in this way show an opposite trend with azimuthal angle for the two Fermi sheets. For the β band, we observe a gentle decrease of v_F as we approach the ΓX direction, whereas for γ, the velocity increases by more than a factor of 2 over the same range [57]. This provides a first indication for a strong momentum dependence of the self-energies $\Sigma'_{\beta,\gamma}$, which we analyze quantitatively in Sec. V. Here, we limit the discussion to the angle dependence of the mass enhancement v_b/v_F, which we calculate from the measured quasiparticle Fermi velocities of Fig. 2(c) and the corresponding bare velocities v_b of a reference Hamiltonian $\hat{H}^0$ defined in Sec. IV. As shown in Fig. 2(d), this confirms a substantial many-body effect on

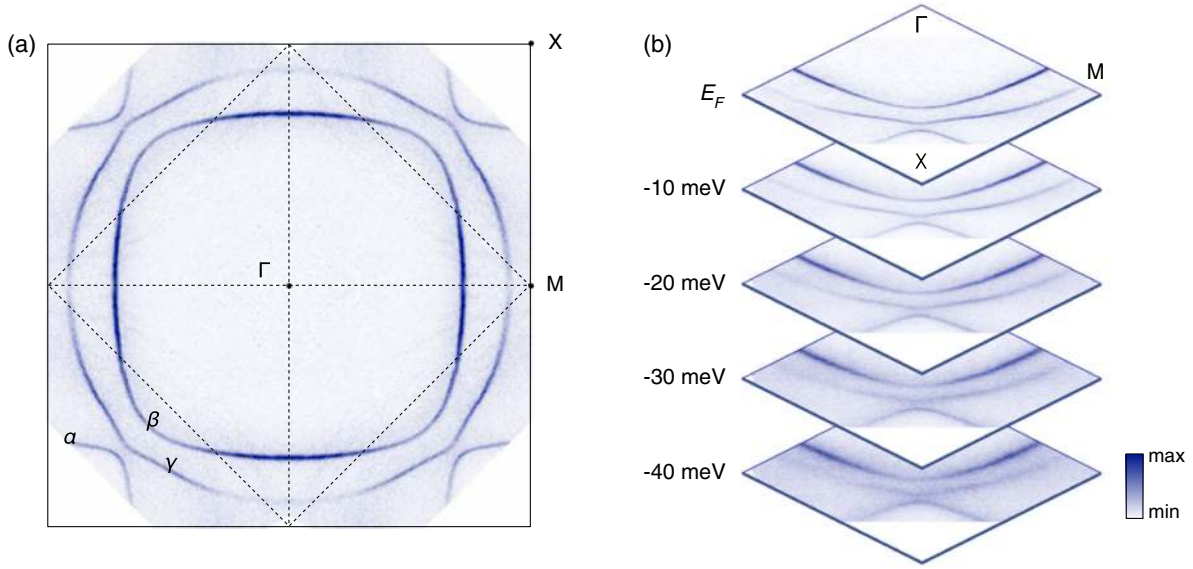

FIG. 1. (a) Fermi surface of Sr_2RuO_4. The data were acquired at 5 K on a CO passivated surface with a photon energy of 11 eV and p polarization for measurements along the ΓX symmetry line. The sample tilt around the ΓX axis used to measure the full Fermi surface results in a mixed polarization for data away from this symmetry axis. The Brillouin zone of the reconstructed surface layer is indicated by diagonal dashed lines. Surface states and final-state umklapp processes are suppressed to near the detection limit. A comparison with ARPES data from a pristine cleave is shown in the Appendix A. The data in panel (a) have been mirror symmetrized for clarity. Original measured data span slightly more than a quadrant of the Brillouin zone. (b) Constant energy surfaces illustrating the progressive broadening of the quasiparticle states away from the Fermi level E_F.

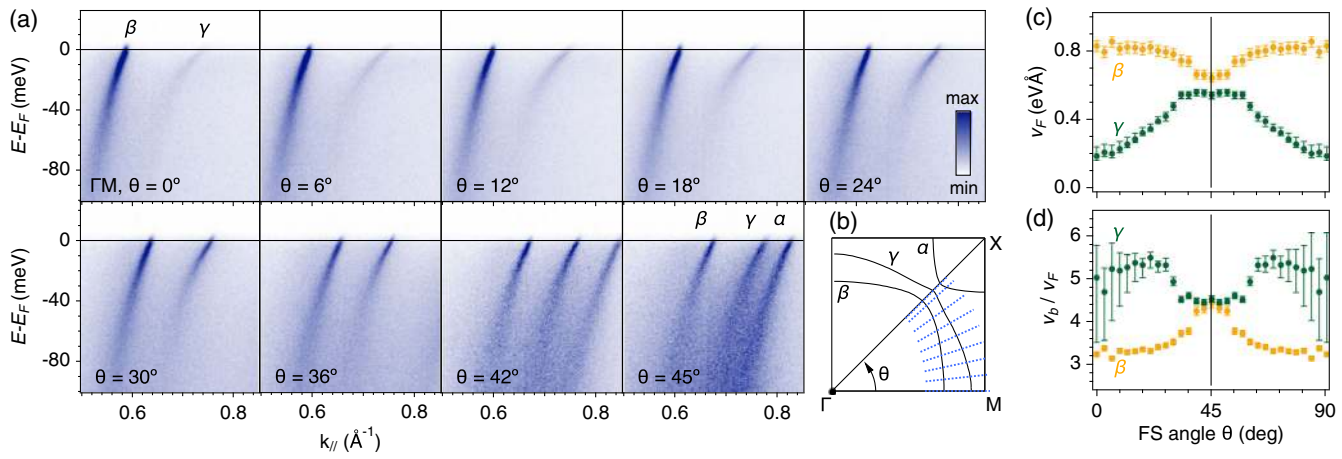

FIG. 2. (a) Quasiparticle dispersions measured with p-polarized light, for different azimuthal angles θ as defined in panel (b). (c) Angular dependence of the quasiparticle velocity v_F along the β and γ Fermi surface sheets. (d) Angular dependence of the quasiparticle mass enhancement v_b/v_F. Here, v_b is the bare velocity obtained from the single-particle Hamiltonian $\hat{H}^0 = \hat{H}^{\mathrm{DFT}} + \hat{H}^{\mathrm{SOC}}_{\lambda_{\mathrm{DFT}}+\Delta\lambda}$ defined in Sec. IV, and v_F is the quasiparticle Fermi velocity measured by ARPES. Error bars are obtained by propagating the experimental uncertainty on v_F.

the anisotropy of the quasiparticle dispersion. Along ΓM, we find a strong differentiation with mass enhancements of about 5 for the γ sheet and 3.2 for β, whereas v_b/v_F approaches a common value of approximately 4.4 for both sheets along the Brillouin zone diagonal.

Before introducing the theoretical framework used to quantify the anisotropy of the self-energy and the effects of SOC, we compare our data quantitatively to bulk sensitive quantum oscillation measurements. Using the experimental Fermi wave vectors $\boldsymbol{k}_F$ and velocities determined from our data on a dense grid along the entire Fermi surface, we can compute the cyclotron masses measured by de Haas-van Alphen experiments, without relying on the approximation of circular Fermi surfaces and/or isotropic Fermi velocities used in earlier studies [33,49,56,58]. Expressing the cyclotron mass m^* as

$$m^* = \frac{\hbar^2}{2\pi}\frac{\partial A_{\mathrm{FS}}}{\partial \epsilon} = \frac{\hbar^2}{2\pi}\int_0^{2\pi} \frac{k_F(\theta)}{\partial\epsilon/\partial k(\theta)}\, d\theta, \tag{1}$$

where A_{FS} is the Fermi surface volume, and using the data shown in Fig. 2(c), we obtain $m^*_\gamma = 17.3(2.0)m_e$ and $m^*_\beta = 6.1(1.0)m_e$, in quantitative agreement with the values of $m^*_\gamma = 16\ m_e$ and $m^*_\beta = 7\ m_e$ found in de Haas-van Alphen experiments [12,25,26]. We thus conclude that the quasiparticle states probed by our experiments are representative of the bulk of Sr_2RuO_4 [59].

III. THEORETICAL FRAMEWORK

In order to define the electronic self-energy and assess the effect of electronic correlations in the spectral function measured by ARPES, we need to specify a one-particle Hamiltonian $\hat{H}^0$ as a reference point. At this stage, we keep the presentation general. The particular choice of $\hat{H}^0$ will be a focus of Sec. IV. The eigenstates $|\psi_\nu(\boldsymbol{k})\rangle$ of $\hat{H}^0(\boldsymbol{k})$ at a given quasimomentum $\boldsymbol{k}$ and the corresponding eigenvalues $\varepsilon_\nu(\boldsymbol{k})$ define the "bare" band structure of the system, with respect to which the self-energy $\Sigma_{\nu\nu'}(\omega,\boldsymbol{k})$ is defined in the standard way from the interacting Green's function

$$G^{-1}_{\nu\nu'}(\omega,\boldsymbol{k}) = (\omega + \mu - \varepsilon_\nu(\boldsymbol{k}))\delta_{\nu\nu'} - \Sigma_{\nu\nu'}(\omega,\boldsymbol{k}). \tag{2}$$

In this expression, ν and ν' label the bands and ω denotes the energy counted from E_F. The interacting value of the chemical potential μ sets the total electron number. Since μ can be conventionally included in $\hat{H}^0$, we omit it in the following.

The Fermi surfaces and dispersion relations of the quasiparticles are obtained as the solutions $\omega = 0$ and $\omega = \omega^{\mathrm{QP}}_\nu(\boldsymbol{k})$ of

$$\det\left[(\omega - \varepsilon_\nu(\boldsymbol{k}))\delta_{\nu\nu'} - \Sigma'_{\nu\nu'}(\omega,\boldsymbol{k})\right] = 0. \tag{3}$$

In the above equation, Σ' denotes the real part of the self-energy. Its imaginary part Σ'' has been neglected; i.e., we assume that quasiparticles are coherent with a lifetime longer than $1/\omega^{\mathrm{QP}}$. Our data indicate that this is indeed the case up to the highest energies analyzed here. At very low frequency, the lifetime of quasiparticles cannot be reliably tested by ARPES since the intrinsic quasiparticle width is masked by contributions of the experimental resolution, impurity scattering and inhomogeneous broadening. However, the observation of strong quantum oscillations in the bulk provides direct

evidence for well-defined quasiparticles in Sr_2RuO_4 down to the lowest energies [25,27].

It is important to note that the Green's function G, the self-energy Σ, and the spectral function A are, in general, nondiagonal matrices. This aspects has been overlooked thus far in self-energy analyses of ARPES data, but it is essential to determine the nature of many-body interactions in Sr_2RuO_4, as we show in Sec. V.

A. Localized orbitals and electronic structure

Let us recall some of the important aspects of the electronic structure of Sr_2RuO_4. As shown in Sec. II B, three bands, commonly denoted $\nu = \{\alpha, \beta, \gamma\}$, cross the Fermi level. These bands correspond to states with t_{2g} symmetry derived from the hybridization between localized Ru-4d (d_{xy}, d_{yz}, d_{xz}) orbitals and O-2p states. Hence, we introduce a localized basis set of t_{2g}-like orbitals $|\chi_m\rangle$, with basis functions conveniently labeled as $m = \{xy, yz, xz\}$. In practice, we use maximally localized Wannier functions [60,61] constructed from the Kohn-Sham eigenbasis of a non-SOC density functional theory (DFT) calculation (see Appendix B 1 for details). We term the corresponding Hamiltonian $\hat{H}^{\mathrm{DFT}}$. It is important to note that the choice of a localized basis set is not unique, and other ways of defining these orbitals are possible (see, e.g., Ref. [62]).

In the following, this set of orbitals plays two important roles. First, they are atom centered and provide a set of states localized in real space $|\chi_m(\mathbf{R})\rangle$. Second, the unitary transformation matrix to the band basis $|\psi_\nu(\boldsymbol{k})\rangle$,

$$U_{m\nu}(\boldsymbol{k}) = \langle \chi_{km} | \psi_{k\nu} \rangle, \tag{4}$$

allows us to define an "orbital" character of each band ν as $|U_{m\nu}(\boldsymbol{k})|^2$. In the localized-orbital basis, the one-particle Hamiltonian is a nondiagonal matrix, which reads

$$\hat{H}^0_{mm'}(\boldsymbol{k}) = \sum_\nu U_{m\nu}(\boldsymbol{k}) \varepsilon_\nu(\boldsymbol{k}) U^*_{m'\nu}(\boldsymbol{k}). \tag{5}$$

The self-energy in the orbital basis is expressed as

$$\Sigma_{mm'}(\omega, \boldsymbol{k}) = \sum_{\nu\nu'} U_{m\nu}(\boldsymbol{k}) \Sigma_{\nu\nu'}(\omega, \boldsymbol{k}) U^*_{m'\nu'}(\boldsymbol{k}), \tag{6}$$

and conversely in the band basis as

$$\Sigma_{\nu\nu'}(\omega, \boldsymbol{k}) = \sum_{mm'} U^*_{m\nu}(\boldsymbol{k}) \Sigma_{mm'}(\omega, \boldsymbol{k}) U_{m'\nu'}(\boldsymbol{k}). \tag{7}$$

B. Spin-orbit coupling

We treat SOC as an additional term to $\hat{H}^{\mathrm{DFT}}$, which is independent of $\boldsymbol{k}$ in the localized-orbital basis but leads to a mixing of the individual orbitals. The single-particle SOC term for atomic d orbitals projected to the t_{2g} subspace reads [63]

$$\hat{H}^{\mathrm{SOC}}_\lambda = \frac{\lambda}{2} \sum_{mm'} \sum_{\sigma\sigma'} c^\dagger_{m\sigma} (\mathbf{l}_{mm'} \cdot \boldsymbol{\sigma}_{\sigma\sigma'}) c_{m'\sigma'}, \tag{8}$$

where $\mathbf{l}$ are the t_{2g}-projected angular-momentum matrices, $\boldsymbol{\sigma}$ are Pauli matrices, and λ will be referred to in the following as the SOC coupling constant. As documented in Appendix B 1, the eigenenergies of a DFT + SOC calculation are well reproduced by $\hat{H}^{\mathrm{DFT}} + \hat{H}^{\mathrm{SOC}}_\lambda$ with $\lambda_{\mathrm{DFT}} = 100$ meV.

IV. ENHANCED EFFECTIVE SPIN-ORBIT COUPLING AND SINGLE-PARTICLE HAMILTONIAN

The importance of SOC for the low-energy physics of Sr_2RuO_4 has been pointed out by several authors [8,17,21,23,31,64–68]. SOC lifts degeneracies found in its absence and causes a momentum-dependent mixing of the orbital composition of quasiparticle states, which has nontrivial implications for superconductivity [8,17,68]. Signatures of SOC have been detected experimentally on the Fermi surface of Sr_2RuO_4 in the form of a small protrusion of the γ sheet along the zone diagonal [31,66] and as a degeneracy lifting at the band bottom of the β sheet [68]. These studies reported an overall good agreement between the experimental data and the effects of SOC calculated within DFT [31,66,68]. This is in apparent contrast to more recent DMFT studies of Sr_2RuO_4, which predict large but frequency-independent off-diagonal contributions to the local self-energy that can be interpreted as a contribution $\Delta\lambda$ to the effective coupling strength $\lambda^{\mathrm{eff}} = \lambda_{\mathrm{DFT}} + \Delta\lambda$ [21,23]. This result is also consistent with general perturbation-theory considerations [51], which show a Coulomb enhancement of the level splitting in the J basis, similar to a Coulomb-enhanced crystal-field splitting [69].

In the absence of SOC, DFT yields a quasicrossing between the β and γ Fermi surface sheets a few degrees away from the zone diagonal, as displayed in Fig. 3(a). Near such a point, we expect the degeneracy to be lifted by SOC, leading to a momentum splitting $\Delta k = \lambda^{\mathrm{eff}}/v$ and to an energy splitting of $\Delta E = Z\lambda^{\mathrm{eff}}$ [23], as depicted schematically in Fig. 3(e). In these expressions, $v \equiv \sqrt{v_\beta v_\gamma}$, where v_β and v_γ are the bare band velocities in the absence of SOC and correlations, and $Z \equiv \sqrt{Z_\beta Z_\gamma}$ involves the quasiparticle residues Z_ν associated with each band (also in the absence of SOC).

It is clear from these expressions that a quantitative determination of λ_{eff} is not possible from experiment alone. Earlier studies on Sr_2RuO_4 [68] and iron-based superconductors [70] have interpreted the energy splitting ΔE at avoided crossings as a direct measure of the SOC

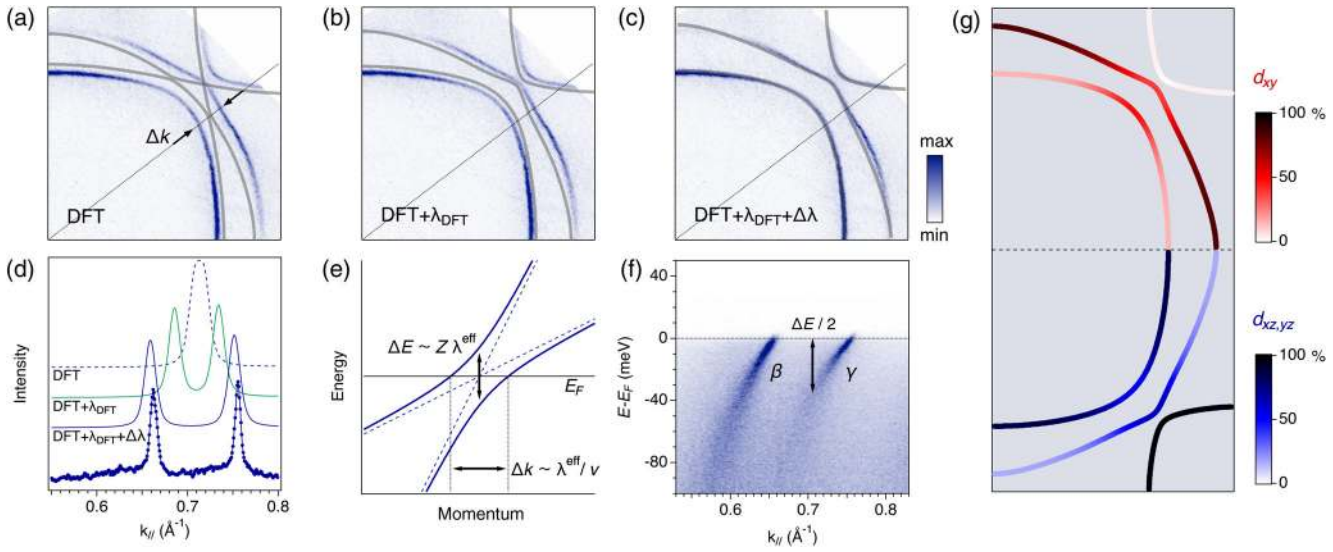

FIG. 3. Correlation enhanced effective SOC. (a) Quadrant of the experimental Fermi surface with a DFT calculation without SOC ($\hat{H}^{\mathrm{DFT}}$) at the experimental $k_z \approx 0.4\pi/c$ (grey lines). (b,c) Same as panel (a), with calculations including SOC ($\mathrm{DFT} + \lambda_{\mathrm{DFT}}$) and enhanced SOC ($\lambda_{\mathrm{DFT}} + \Delta\lambda$), respectively. For details, see the main text. (d) Comparison of the experimental MDC along the $\boldsymbol{k}$-space cut indicated in panel (a) with different calculations shown in panels (a)–(c). (e) Schematic illustration of the renormalization of a SOC-induced degeneracy lifting. Here, $Z = \sqrt{Z_\nu Z_{\nu'}}$, where ν, ν' label the two bands, and $v = \sqrt{v_\nu v_{\nu'}}$, where v_ν, $v_{\nu'}$ are bare velocities in the absence of SOC [23] (see text). (f) Experimental quasiparticle dispersion along the $\boldsymbol{k}$-space cut indicated in panel (a). (g) Orbital character of the $\mathrm{DFT} + \lambda_{\mathrm{DFT}} + \Delta\lambda$ eigenstates along the Fermi surface.

strength λ^{eff}. However, in interacting systems, ΔE is not a robust measure of SOC since correlations can both enhance ΔE by enhancing λ_{eff} and reduce it via the renormalization factor Z. We thus quantify the enhancement of SOC from the momentum splitting Δk, which is not renormalized by the quasiparticle residue Z. The experimental splitting at the avoided crossing between the β and γ Fermi surface sheets indicated in Fig. 3(a) is $\Delta k^{\mathrm{QP}} = 0.094(9)$ Å^{-1}, whereas DFT predicts $\Delta k^{\mathrm{DFT}+\lambda_{\mathrm{DFT}}} = 0.046$ Å^{-1}. We thus obtain an effective SOC strength $\lambda^{\mathrm{eff}} = \lambda_{\mathrm{DFT}} \Delta k^{\mathrm{QP}} / \Delta k^{\mathrm{DFT}+\lambda_{\mathrm{DFT}}} = 205(20)$ meV, in quantitative agreement with the predictions in Refs. [21,23]. We note that despite this large enhancement of the effective SOC, the energy splitting remains smaller than λ_{DFT}, as shown in Fig. 3(f). When deviations from linearity in band dispersions are small, the splitting ΔE is symmetric around the E_F and can thus be determined from the occupied states probed in experiment. Direct inspection of the data in Fig. 3(f) yields $\Delta E \approx 70$ meV, which is about $2/3$ of λ_{DFT} and thus clearly not a good measure of SOC.

The experimental splitting is slightly larger than that expected from the expression $\Delta E = Z\lambda^{\mathrm{eff}}$ and our theoretical determination of Z_β and Z_γ at the Fermi surface (which will be described in Sec. VI). This discrepancy can be attributed to the energy dependence of Z, which, in Sr_2RuO_4, is not negligible over the energy scale of SOC. Note that the magnitude of the SOC-induced splitting of the bands at the Γ point reported in Ref. [68] can also be explained by the competing effects of enhancement by correlations and reduction by the quasiparticle weight as shown in Ref. [23]. We also point out that the equilibration of quasiparticle velocities close to the diagonal, apparent from Figs. 2(a), 2(c), and 3(f), is indeed the behavior expected close to an avoided crossing [23].

Including the enhanced SOC determined from this noncrossing gap leads to a much-improved theoretical description of the entire Fermi surface [71]. As shown in Fig. 3(b), our high-resolution experimental Fermi surface deviates systematically from a DFT calculation with SOC. Most notably, $\hat{H}^{\mathrm{DFT}} + \hat{H}^{\mathrm{SOC}}_{\lambda_{\mathrm{DFT}}}$ underestimates the size of the γ sheet and overestimates the β sheet. Intriguingly, this is almost completely corrected in $\hat{H}^{\mathrm{DFT}} + \hat{H}^{\mathrm{SOC}}_{\lambda_{\mathrm{DFT}}+\Delta\lambda}$, with $\lambda_{\mathrm{DFT}} + \Delta\lambda = 200$ meV, as demonstrated in Fig. 3(c). Indeed, a close inspection shows that the remaining discrepancies between experiment and $\hat{H}^{\mathrm{DFT}} + \hat{H}^{\mathrm{SOC}}_{\lambda_{\mathrm{DFT}}+\Delta\lambda}$ break the crystal symmetry, suggesting that they are dominated by experimental artifacts. A likely source for these image distortions is imperfections in the electron optics arising from variations of the work function around the electron emission spot on the sample. Such distortions cannot presently be fully eliminated in low-energy photoemission from cleaved single crystals.

Importantly, the change in Fermi surface sheet volume with the inclusion of $\Delta\lambda$ is not driven by a change in the crystal-field splitting between the xy and xz, yz orbitals (see Appendix B 1). The volume change occurs solely because

of a further increase in the orbital mixing induced by the enhanced SOC. As shown in Fig. 3(g), this mixing is not limited to the vicinity of the avoided crossing but extends along the entire Fermi surface (see Fig. 10 in Appendix B 1 for the orbital character without SOC). For $\lambda_{\mathrm{DFT}}+\Delta\lambda$, we find a minimal d_{xy} and $d_{xz,yz}$ mixing for the γ and β bands of 20%/80% along the ΓM direction with a monotonic increase to approximately 50% along the Brillouin zone diagonal ΓX. We note that this mixing varies with the perpendicular momentum k_z. However, around the experimental value of $k_z \approx 0.4\pi/c$, the variation is weak [73]. The analysis presented here and in Secs. II B and VI is thus robust with respect to a typical uncertainty in k_z. These findings suggest that a natural reference single-particle Hamiltonian is $\hat{H}^0 = \hat{H}^{\mathrm{DFT}} + \hat{H}^{\mathrm{SOC}}_{\lambda_{\mathrm{DFT}}+\Delta\lambda}$. This choice ensures that the Fermi surface of $\hat{H}^0$ is very close to that of the interacting system. From Eq. (3), this implies that the self-energy matrix approximately vanishes at zero binding energy: $\Sigma'_{\nu\nu'}(\omega=0,\boldsymbol{k}) \simeq 0$. We choose $\hat{H}^0$ in this manner in all of the following. Hence, from now on, $|\psi_\nu(\boldsymbol{k})\rangle$ and $\varepsilon_\nu(\boldsymbol{k})$ refer to the eigenstates and band structure of $\hat{H}^0 = \hat{H}^{\mathrm{DFT}} + \hat{H}^{\mathrm{SOC}}_{\lambda_{\mathrm{DFT}}+\Delta\lambda}$. We point out that although $\hat{H}^0$ is a single-particle Hamiltonian, the effective enhancement $\Delta\lambda$ of SOC included in $\hat{H}^0$ is a correlation effect beyond DFT.

V. EXPERIMENTAL DETERMINATION OF SELF-ENERGIES

A. Self-energies in the band basis

Working in the band basis, i.e., with the eigenstates of $\hat{H}^0$, the maximum of the ARPES intensity for a given binding energy ω (maximum of the MDCs) corresponds to the momenta $\boldsymbol{k}$ that satisfy [following Eq. (3)] $\omega - \varepsilon_\nu(\boldsymbol{k}) - \Sigma'_{\nu\nu}(\omega,\boldsymbol{k}) = 0$. Hence, for each binding energy, each azimuthal cut, and each sheet of the quasiparticle dispersions, we fit the MDCs and determine the momentum $\boldsymbol{k}^\nu_{\max}(\omega)$ at their maximum. Using the value of $\varepsilon_\nu(\boldsymbol{k}^\nu_{\max}(\omega))$ at this momentum yields the following quantity:

$$\omega - \varepsilon_\nu(\boldsymbol{k}^\nu_{\max}(\omega)) = \Sigma'_{\nu\nu}(\omega,\boldsymbol{k}^\nu_{\max}(\omega)) \equiv \Sigma'_\nu(\omega,\theta). \quad (9)$$

This equation corresponds to the simple construction illustrated graphically in Fig. 4(b), and it is a standard way of extracting a self-energy from ARPES, as used in previous works on several materials [32,48,74–76]. We note that this procedure assumes that the off-diagonal components $\Sigma'_{\nu\neq\nu'}(\omega,\boldsymbol{k})$ can be neglected for states close to the Fermi surface (i.e., for small ω and $\boldsymbol{k}$ close to a Fermi crossing). This assumption can be validated, as shown in Appendix C. When performing this analysis, we only include the α sheet for $\theta = 45°$. Whenever the constraint

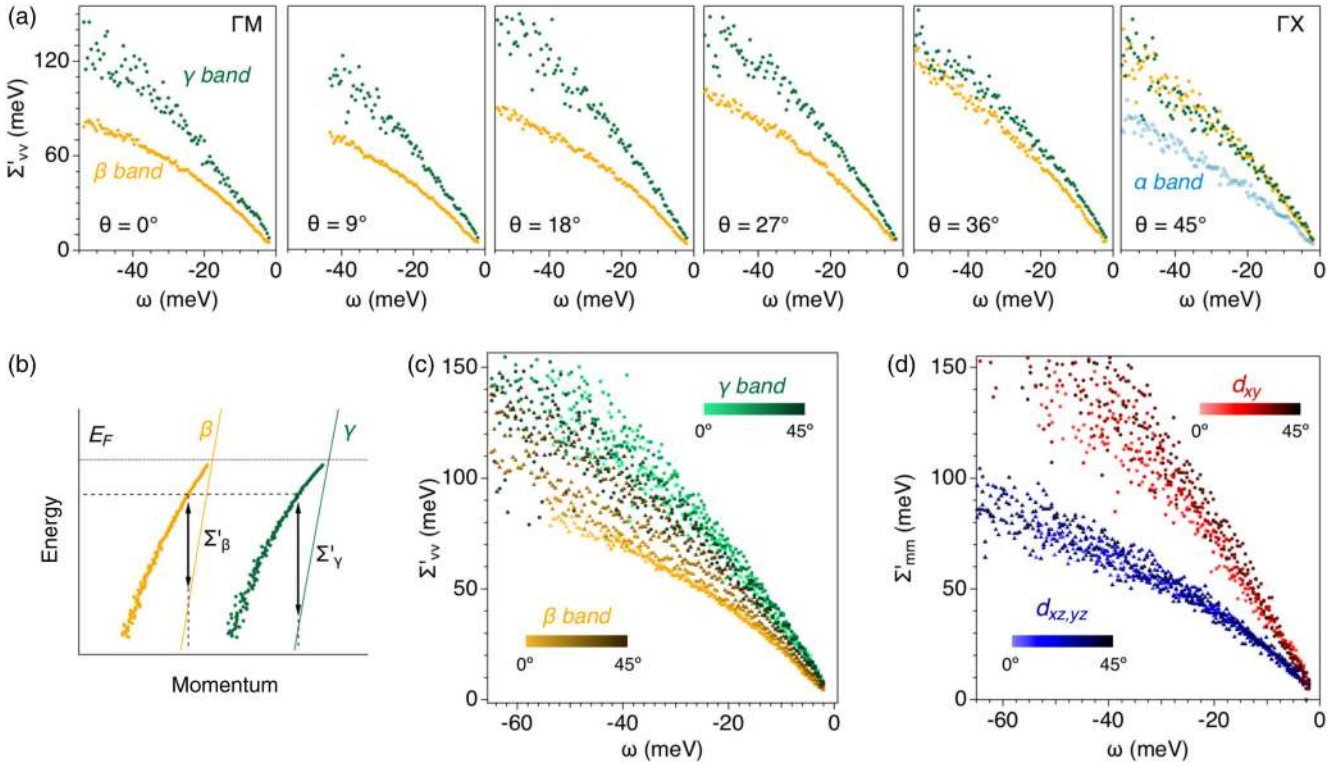

FIG. 4. Self-energies extracted in the band and orbital bases. (a) Real part of the self-energy $\Sigma'_{\nu\nu}$ in the band basis (solid symbols) in 9° steps of the Fermi surface angle θ. (b) Illustration of the relation between $\Sigma'_{\nu\nu}$, the bare bands given by $\hat{H}^0$ (thin lines), and the quasiparticle peak positions (solid symbols). (c) Compilation of $\Sigma'_{\nu\nu}$ from panel (a). (d) Real part of the self-energy Σ'_{mm} in the orbital basis.

$\Sigma'_\nu(\omega \to 0) \to 0$ on the self-energy is not precisely obeyed, a small shift is applied to set it to zero. We chose this procedure to correct for the minor differences between the experimental and the reference $\hat{H}^0$ Fermi wave vectors because we attribute these differences predominantly to experimental artifacts.

The determined self-energies for each band $\nu = \alpha, \beta, \gamma$ and the different values of θ are depicted in Figs. 4(a) and 4(c). For the β and γ sheets, they show a substantial dependence on the azimuthal angle. Around ΓM, we find that Σ'_γ exceeds Σ'_β by almost a factor of 2 (at $\omega = -50$ meV), whereas they essentially coincide along the zone diagonal (ΓX). This change evolves as a function of θ and occurs via a simultaneous increase in Σ'_β and a decrease in Σ'_γ for all energies as θ is increased from 0° (ΓM) to 45° (ΓX). In order to better visualize this angular dependence, a compilation of $\Sigma'_\nu(\omega)$ for different values of θ is displayed in Fig. 4(c).

B. Accounting for the angular dependence: Local self-energies in the orbital basis

In this section, we introduce a different procedure for extracting self-energies from ARPES, by working in the orbital basis $|\chi_m(\boldsymbol{k})\rangle$. We do this by making two key assumptions:

(1) We assume that the off-diagonal components are negligible, i.e., $\Sigma'_{m\neq m'} \simeq 0$. Let us note that in Sr_2RuO_4, even a $\boldsymbol{k}$-independent self-energy has nonzero off-diagonal elements if $\hat{H}^{\mathrm{DFT}} + \hat{H}^{\mathrm{SOC}}_{\lambda_{\mathrm{DFT}}}$ is considered. Using DMFT, these off-diagonal elements have been shown to be very weakly dependent on frequency in this material [23], leading to the notion of a static correlation enhancement of the effective SOC ($\Delta\lambda$). In the present work, these off-diagonal frequency-independent components are already incorporated into $\hat{H}^0$ (see Sec. IV), and thus the frequency-dependent part of the self-energy is (approximately) orbital diagonal by virtue of the tetragonal crystal structure.

(2) We assume that the diagonal components of the self-energy in the orbital basis depend on the momentum $\boldsymbol{k}$ only through the azimuthal angle $\theta_{\boldsymbol{k}}$: $\Sigma'_{mm}(\omega, \boldsymbol{k}) \simeq \Sigma'_m(\omega, \theta_{\boldsymbol{k}})$. We neglect the dependence on the momentum, which is parallel to the angular cut.

Under these assumptions, the equation determining the quasiparticle dispersions reads

$$\det[(\omega - \Sigma'_m(\omega, \theta_{\boldsymbol{k}}))\delta_{mm'} - \hat{H}^0_{mm'}(\boldsymbol{k})] = 0. \quad (10)$$

In this equation, we have neglected the lifetime effects associated with the imaginary part Σ''_m. In order to extract the functions $\Sigma'_m(\omega, \theta_{\boldsymbol{k}})$ directly from the ARPES data, we first determine the peak positions $\boldsymbol{k}^\nu_{\mathrm{max}}(\omega, \theta)$ for MDCs at a given angle θ and binding energy ω. We then compute (for the same ω and θ) the matrix $A_{mm'} \equiv \omega\delta_{mm'} - \hat{H}^0_{mm'}(\boldsymbol{k}^\alpha_{\mathrm{max}}(\omega, \theta_{\boldsymbol{k}}))$ and similarly $B_{mm'}$, $G_{mm'}$ for the β and γ band MDCs, $\boldsymbol{k}^\beta_{\mathrm{max}}(\omega, \theta)$ and $\boldsymbol{k}^\gamma_{\mathrm{max}}(\omega, \theta)$, respectively. In terms of these matrices, the quasiparticle equations (10) read

$$\begin{aligned}\det[A_{mm'} - \Sigma'_m\delta_{mm'}] &= \det[B_{mm'} - \Sigma'_m\delta_{mm'}] \\ &= \det[G_{mm'} - \Sigma'_m\delta_{mm'}] = 0. \quad (11)\end{aligned}$$

However, when taking symmetry into account, the self-energy has only two independent components: Σ'_{xy} and $\Sigma'_{xz} = \Sigma'_{yz}$. Hence, we only need two of the above equations to solve for the two unknown components of the self-energy. This means that we can also extract a self-energy in the directions where only two bands (β and γ) are present in the considered energy range of $\omega \lesssim 100$ meV, e.g., along ΓM. The resulting functions $\Sigma'_m(\omega, \theta_{\boldsymbol{k}})$ determined at several angles θ are displayed in Fig. 4(d). It is immediately apparent that, in contrast to $\Sigma'_{\nu\nu}$, the self-energies in the orbital basis do not show a strong angular (momentum) dependence, but rather, they collapse into two sets of points, one for the xy orbital and one for the xz/yz orbitals. Thus, we reach the remarkable conclusion that the angular dependence of the self-energy in the orbital basis is negligible, within the range of binding energies investigated here: $\Sigma'_m(\omega, \theta_{\boldsymbol{k}}) \simeq \Sigma'_m(\omega)$. This result implies that a good approximation of the full momentum and energy dependence of the self-energy in the band (quasiparticle) basis is given by

$$\Sigma_{\nu\nu'}(\omega, \boldsymbol{k}) = \sum_m U^*_{m\nu}(\boldsymbol{k})\Sigma_m(\omega)U_{m\nu'}(\boldsymbol{k}). \quad (12)$$

The physical content of this expression is that the angular (momentum) dependence of the quasiparticle self-energies emphasized above is actually due to the matrix elements $U_{m\nu}(\boldsymbol{k})$ defined in Eq. (4). In Sr_2RuO_4, the angular dependence of these matrix elements is mainly due to the SOC, as seen from the variation of the orbital content of quasiparticles in Fig. 3(g). In Appendix D, we show the back-transform of $\Sigma'_m(\omega, \theta_{\boldsymbol{k}} = 18°)$ into $\Sigma'_\nu(\omega, \theta_{\boldsymbol{k}} = 0, 18, 45°)$. The good agreement with $\Sigma'_{\nu\nu}$ directly extracted from experiment further justifies the above expression and also confirms the validity of the approximations made throughout this section.

Finally, we stress that expression (12) precisely coincides with the *ansatz* made by DMFT: Within this theory, the self-energy is approximated as a local ($\boldsymbol{k}$-independent) object when expressed in a basis of localized orbitals, while it acquires momentum dependence when transformed to the band basis.

VI. COMPARISON TO DYNAMICAL MEAN-FIELD THEORY

In this section, we perform an explicit comparison of the measured quasiparticle dispersions and self-energies to DMFT results. The latter are based on the Hamiltonian

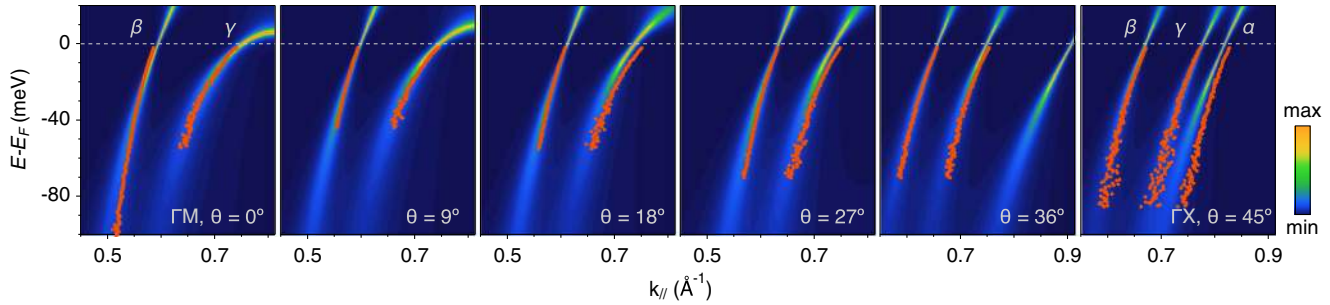

FIG. 5. Comparison of experimental quasiparticle dispersions (markers) with DMFT spectral functions (color plots) calculated for different Fermi surface angles θ.

$\hat{H}^{\mathrm{DFT}}$, to which the Hubbard-Kanamori interaction with on-site interaction $U = 2.3$ eV and Hund's coupling $J = 0.4$ eV [20] is added. For the details of the DMFT calculation and especially the treatment of SOC in this framework, we refer the reader to Appendix B. There, we also comment on some of the limitations and shortcomings of the current state of the art for DFT + DMFT calculations in this context. Figure 5(a) shows the experimental quasiparticle dispersion extracted from our ARPES data (circles) on top of the DMFT spectral function $A(\omega, \boldsymbol{k})$ displayed as a color-intensity map. Clearly, the theoretical results are in near quantitative agreement with the data: Both the strong renormalization of the Fermi velocity and the angular-dependent curvature of the quasiparticle bands are very well reproduced by the purely local, and thus momentum-independent, DMFT self-energies. This result validates the assumption of no momentum dependence along the radial k-space direction of the self-energy made in Sec. V B for the k/ω range studied here. The small deviations in Fermi wave vectors discernible in Fig. 5 are consistent with Fig. 3(c) and the overall experimental precision of the Fermi surface determination.

In Fig. 6(a), we compare the experimental self-energies for each orbital with the DMFT results. The overall agreement is notable. At low energy, the self-energies are linear in frequency, and the agreement is excellent. The slope of the self-energies in this regime controls the angular dependence of the effective mass renormalization. Using the local ansatz (12) in the quasiparticle dispersion equation and performing an expansion around E_F, we obtain

$$\frac{v_b}{v_F^{\nu}(\theta)} = \sum_m \frac{1}{Z_m} |U_{m\nu}(\theta)|^2, \qquad \frac{1}{Z_m} \equiv 1 - \left.\frac{\partial \Sigma'_m}{\partial \omega}\right|_{\omega=0}. \quad (13)$$

In Fig. 6(b), we show $v_b/v_F^{\nu}(\theta)$ for the β and γ bands using the DMFT values $Z_{xy} = 0.18 \pm 0.01$ and $Z_{xz/yz} = 0.30 \pm 0.01$ obtained at 29 K (Appendix B 2). The overall angular dependence and the absolute value of the γ band mass enhancement is very well captured by DMFT, while the β band is a bit overestimated. Close to the zone diagonal

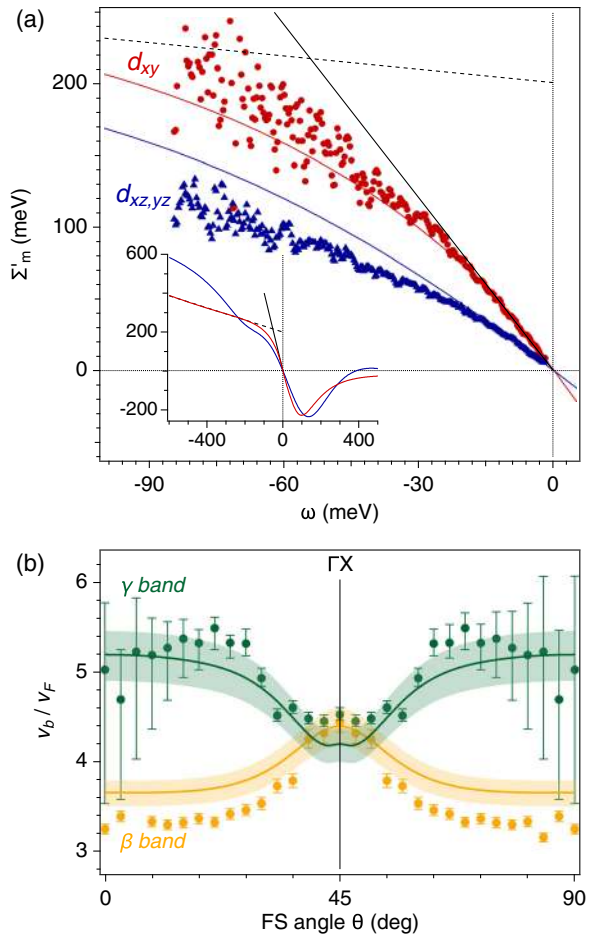

FIG. 6. (a) Average of the self-energies $\Sigma'_{xz/yz}$, Σ'_{xy} shown in Fig. 4(d) compared with DMFT self-energies calculated at 29 K. The self-energies are shifted such that $\Sigma'_m(\omega = 0) = 0$. The inset shows the DMFT self-energies over a larger energy range. Linear fits at low and high energies of Σ'_{xy} from DMFT are shown as solid and dashed black lines, respectively. (b) Angle dependence of the mass enhancement v_b/v_F from ARPES (markers) and DMFT (solid line). The range indicated by the shaded areas corresponds to mass enhancements calculated from the numerical data by using different methods (see Appendix B 2). Error bars on the experimental data are obtained from propagating the estimated uncertainty of the Fermi velocities shown in Fig. 2(c).

($\theta = 45°$), the two mass enhancements are approximately equal, due to the strong orbital mixing induced by the SOC.

Turning to larger binding energies, we see that the theoretical Σ'_{xy} is in good agreement with the experimental data over the full energy range of 2–80 meV covered in our experiments. Both the theoretical and experimental self-energies deviate significantly from the linear regime down to low energies (∼20 meV), causing curved quasiparticle bands with progressively steeper dispersion as the energy increases (Fig. 5). In contrast, the agreement between theory and experiment for the xz/yz self-energy is somewhat less impressive at binding energies larger than about 30 meV. Our DMFT self-energy $\Sigma'_{xz/yz}$ overestimates the strength of correlations in this regime (by 20%–25%), with a theoretical slope larger than the experimental one. Correspondingly, the quasiparticle dispersion is slightly steeper in this regime than the theoretical result, as can also be seen in Fig. 5.

There may be several reasons for this discrepancy. Even while staying in the framework of a local self-energy, we note that the present DMFT calculation is performed with an on-site value of U, which is the same for all orbitals. Earlier cRPA calculations have suggested that this on-site interaction is slightly larger for the xy orbital ($U_{xy} = 2.5$ eV and $U_{xz/yz} = 2.2$ eV) [20], and recent work has advocated the relevance of this for DFT + DMFT calculations of Sr_2RuO_4 [21]. Another possible explanation is that this discrepancy is actually a hint of some momentum-dependent contribution to the self-energy, especially the dependence on the momentum perpendicular to the Fermi surface. We note, in this respect, that the discrepancy is larger for the α, β sheets that have dominant xz/yz character. These orbitals have, in the absence of SOC, a strong one-dimensional character, for which momentum dependence is definitely expected and DMFT is less appropriate. Furthermore, these FS sheets are also the ones associated with nesting and spin-density wave correlations, which are expected to lead to an additional momentum dependence of the self-energy. We further discuss possible contributions of spin fluctuations in Sec. VIII.

VII. KINKS

The self-energies $\Sigma'(\omega)$ shown in Figs. 4 and 6(a) display a fairly smooth curvature, rather than pronounced "kinks." Over a larger range, however, Σ'_{xy} from DMFT does show an energy scale marking the crossover from the strongly renormalized low-energy regime to weakly renormalized excitations. This is illustrated in the inset to Fig. 6(a). Such purely electronic kinks were reported in DMFT calculations of a generic system with Mott-Hubbard sidebands [77] and have been abundantly documented in the theoretical literature since then [13,20,78–81]. In Sr_2RuO_4, they are associated with the crossover from the Fermi-liquid behavior into a more incoherent regime [18,20]. The near quantitative agreement of the frequency dependence of the experimental self-energies $\Sigma'_m(\omega)$ and our single-site DMFT calculation provides strong evidence for the existence of such electronic kinks in Sr_2RuO_4. In addition, it implies that the local DMFT treatment of electronic correlations captures the dominant effects.

Focusing on the low-energy regime of our experimental data, we find deviations from the linear form $\Sigma'(\omega) = \omega(1 - 1/Z)$ characteristic of a Fermi liquid for $|\omega| >$ 20 meV, irrespective of the basis. However, this is only an upper limit for the Fermi-liquid energy scale in Sr_2RuO_4. Despite the improved resolution of our experiments, we cannot exclude an even lower crossover energy to non-Fermi-liquid-like excitations. We note that the crossover temperature of $T_{FL} \approx 25$ K reported from transport and thermodynamic experiments [10–12] indeed suggests a crossover energy scale that is significantly below 20 meV.

The overall behavior of $\Sigma'(\omega)$ including the energy range where we find strong changes in the slope agrees with previous photoemission experiments, which were interpreted as evidence for electron-phonon coupling [29–31,46,48]. Such an interpretation, however, relies on a linear Fermi-liquid regime of electronic correlations over the entire phonon bandwidth of approximately 90 meV [82], which is inconsistent with our DMFT calculations. Moreover, attributing the entire curvature of Σ'_m in our data to electron-phonon coupling would result in unrealistic coupling constants far into the polaronic regime, which is hard to reconcile with the transport properties of Sr_2RuO_4 [10–12]. We also note that a recent scanning tunneling microscope (STM) study reported very strong kinks in the β and γ sheets of Sr_2RuO_4 [49], which is inconsistent with our data. We discuss the reason for this discrepancy in Appendix A.

VIII. DISCUSSION AND PERSPECTIVES

In this article, we have reported on high-resolution ARPES measurements that allow for a determination of the Fermi surface and quasiparticle dispersions of Sr_2RuO_4 with unprecedented accuracy. Our data reveal an enhancement (by a factor of about 2) of the splitting between Fermi surface sheets along the zone diagonal, in comparison to the DFT value. This can be interpreted as a correlation-induced enhancement of the effective SOC, an effect predicted theoretically [21,23,51] and demonstrated experimentally here for this material, for the first time.

Thanks to the improved cleanliness of our data, we have been able to determine the electronic self-energies directly from experiment, using both a standard procedure applied in the band (quasiparticle) basis as well as a novel procedure, introduced in the present article, in the orbital basis. Combining these two approaches, we have

demonstrated that the large angular (momentum) dependence of the quasiparticle self-energies and dispersions can be mostly attributed to the fact that quasiparticle states have an orbital content that is strongly angular dependent, due to the SOC. Hence, assuming self-energies that are frequency dependent but essentially independent of angle (momentum), when considered in the orbital basis, is a very good approximation. This provides a direct experimental validation of the DMFT *ansatz*.

The key importance of atomiclike orbitals in correlated insulators is well established [83,84]. The present work demonstrates that orbitals retain a considerable physical relevance even in a metal in the low-temperature Fermi-liquid regime. Although the band and orbital bases used here are equivalent, our analysis shows that the underlying simplicity in the nature of correlations emerges only when working in the latter and taking into account the orbital origin of quasiparticles. Beyond Sr_2RuO_4, this is an observation of general relevance to multiband metals with strong correlations such as the iron-based superconductors [85,86].

Notwithstanding its success, the excellent agreement of the DMFT results with ARPES data does raise puzzling questions. Sr_2RuO_4 is known to be host to strong magnetic fluctuations [39–42], with a strong peak in its spin response $\chi(\mathbf{Q})$ close to the spin-density wave (SDW) vector $\mathbf{Q} \sim (2\pi/3, 2\pi/3)$, as well as quasiferromagnetic fluctuations that are broader in momentum around $\mathbf{Q} = 0$. Indeed, tiny amounts of substitutional impurities induce long-range magnetic order in this material, of either SDW of ferromagnetic type [87,88]. Hence, it is a prominent open question to understand how these long-wavelength fluctuations affect the physics of quasiparticles in the Fermi-liquid state. Single-site DMFT does not capture this feedback, and the excellent agreement with the overall quasiparticle physics must imply that these effects have a comparatively smaller magnitude than the dominant local effect of correlations (on-site U and especially Hund's J) captured by DMFT. A closely related question is how much momentum dependence is present in the low-energy (Landau) interactions between quasiparticles. These effects are expected to be fundamental for subsequent instabilities of the Fermi liquid, into either the superconducting state in pristine samples or magnetic ordering in samples with impurities. Making progress on this issue is also key to the understanding of the superconducting state of Sr_2RuO_4, for which the precise nature of the pairing mechanism as well as the symmetry of the order parameter are still outstanding open questions [4].

The research data supporting this publication can be accessed at the University of St Andrews Research Portal [102].

ACKNOWLEDGMENTS

The experimental work has been supported by the European Research Council (ERC), the Scottish Funding Council, the UK EPSRC, and the Swiss National Science Foundation (SNSF). Theoretical work was supported by the ERC Grant No. ERC-319286-QMAC and by the SNSF (NCCR MARVEL). The Flatiron Institute is a division of the Simons Foundation. A. G. and M. Z. gratefully acknowledge useful discussions with Gabriel Kotliar, Andrew J. Millis, and Jernej Mravlje.

APPENDIX A: BULK AND SURFACE ELECTRONIC STRUCTURE OF Sr_2RuO_4

In Fig. 7, we compare the data presented in the main text with data from a pristine cleave taken with $h\nu = 21$ eV at the SIS beam line of the Swiss Light Source. This comparison confirms the identification of bulk and surface bands by Shen *et al.* [54]. In particular, we find that the larger β sheet has bulk character. This band assignment is used by the vast majority of subsequent ARPES publications [29–31,33,46,56,89,90], except for Ref. [47], which reports a dispersion with much lower Fermi velocity and a strong kink at 15 meV for the smaller β sheet that we identify as a surface band.

Wang *et al.* [49] have recently probed the low-energy electronic structure of Sr_2RuO_4 by STM. Analyzing quasiparticle interference patterns along the ΓX and ΓM high-symmetry directions, they obtained band dispersions with low Fermi velocities and strong kinks at 10 meV and 37 meV. In Fig. 8, we compare the band dispersion reported by Wang *et al.* with our ARPES data. Along both high-symmetry directions, we find a clear discrepancy with our data, which are in quantitative agreement with bulk de Haas

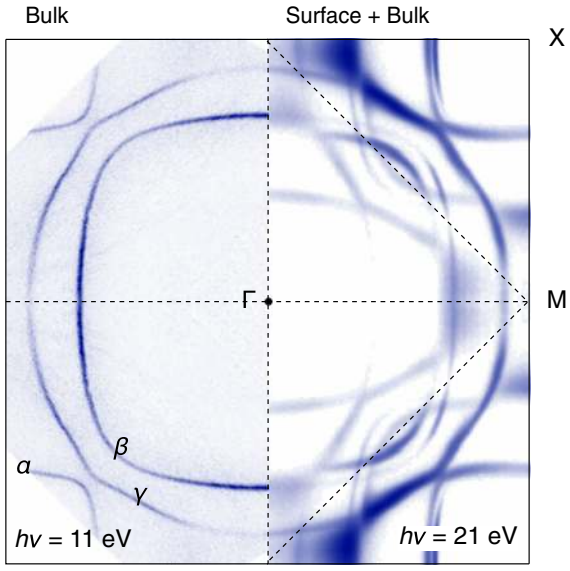

FIG. 7. Bulk and surface electronic structure of Sr_2RuO_4. Left half: Fermi surface map of a CO passivated surface shown in the main text. Right half: Fermi surface acquired on a pristine cleave at 21 eV photon energy. Intense surface states are evident in addition to the bulk bands observed in the left panel.

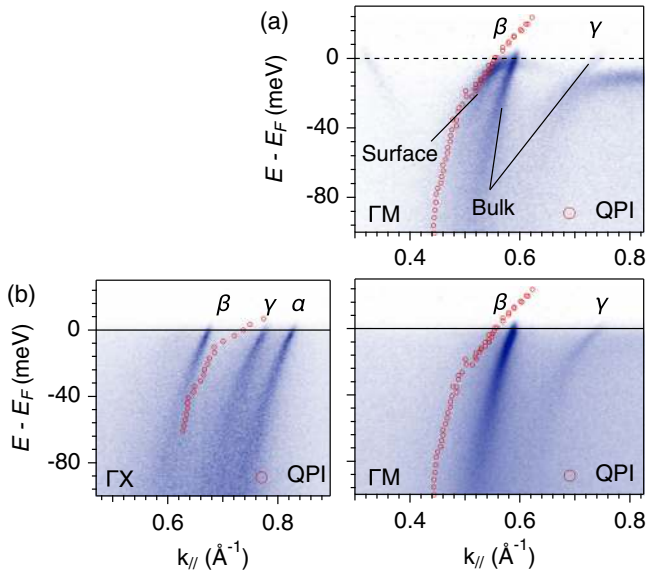

FIG. 8. Comparison with the STM data from Ref. [49]. (a) ΓM high-symmetry cut on a pristine cleave. The bulk β and γ and the surface β bands are labeled. (b) Laser-ARPES data from CO passivated surface showing the bulk band dispersion along ΓX and ΓM. The dispersion obtained from quasiparticle interference in Ref. [49] is overlaid with red markers.

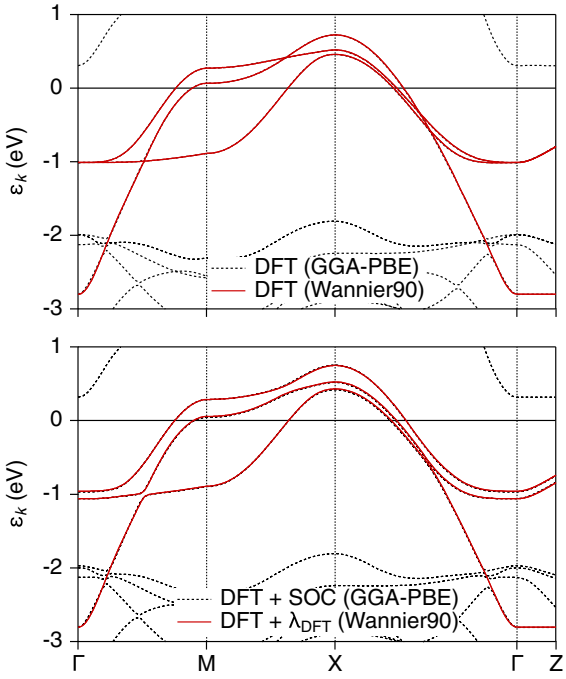

FIG. 9. DFT band structure along the high-symmetry path ΓMXΓZ compared to the eigenstates of our maximally localized Wannier Hamiltonian $\hat{H}^{\mathrm{DFT}}$ for the three t_{2g} bands. Top panel: DFT (GGA-PBE) and eigenstates of $\hat{H}^{\mathrm{DFT}}$. Bottom panel: DFT + SOC (GGA-PBE) and eigenstates of $\hat{H}^{\mathrm{DFT}} + \hat{H}^{\mathrm{SOC}}_{\lambda_{\mathrm{DFT}}}$, with a local SOC term [Eq. (8)] and a coupling strength of $\lambda_{\mathrm{DFT}} = 100$ meV.

van Alphen measurements, as demonstrated in the main text. On the other hand, we find a striking similarity between the STM data along ΓM and the band commonly identified as the surface β band [30,54]. We thus conclude that the experiments reported in Ref. [49] probed the surface states of Sr_2RuO_4. This is fully consistent with the strong low-energy kinks and overall enhanced low-energy renormalization seen by ARPES in the surface bands [50,91].

APPENDIX B: COMPUTATIONAL DETAILS

1. DFT and model Hamiltonian

We generate our theoretical model Hamiltonian $\hat{H}^{\mathrm{DFT}}$ with a maximally localized Wannier function [60,61] construction of t_{2g}-like orbitals for the three bands crossing the Fermi surface. These Wannier orbitals are obtained on a $10 \times 10 \times 10$ $\boldsymbol{k}$ grid based on a non-SOC DFT calculation using WIEN2k [92] with the GGA-PBE functional [93], wien2wannier [94], and Wannier90 [95]. The DFT calculation is performed with lattice parameters from Ref. [96] (measured at 100 K) and converged with twice as many $\boldsymbol{k}$ points in each dimension.

The Wannier orbitals are centered on the Ru atoms and have t_{2g} symmetry but are indeed linear combinations of Ru-d and O-p states. We do not add Wannier functions centered on the oxygen atoms because the resulting three-orbital Wannier model already accurately reproduces the three bands crossing the Fermi energy, as demonstrated in Fig. 9. Also note that the Wannier function construction allows us to disentangle the γ band from the bands with dominantly O-p character below -2 eV.

Note that in the absence of SOC, the eigenstates retain pure orbital character, as shown in Fig. 10. To take SOC into account, we add the local single-particle term $\hat{H}^{\mathrm{SOC}}_{\lambda}$, as given in Eq. (8), with coupling constant λ. In the bottom panel of Fig. 9, we show that the eigenenergies of $\hat{H}^{\mathrm{DFT}} + \hat{H}^{\mathrm{SOC}}_{\lambda}$ are in nearly perfect agreement with the DFT + SOC band structure at a value of $\lambda_{\mathrm{DFT}} = 100$ meV.

Our model Hamiltonian provides the reference point to which we define a self-energy, but it is also a perfect playground to study the change in the Fermi surface under the influence of SOC and the crystal-field splitting between the xy and xz/yz orbitals. In the following, we confirm that the best agreement with the experimental Fermi surface is found with an effective SOC of $\lambda^{\mathrm{eff}} = \lambda_{\mathrm{DFT}} + \Delta\lambda = 200$ meV, but at the same time, we keep the DFT crystal-field splitting of $\epsilon_{\mathrm{cf}} = \epsilon_{xz/yz} - \epsilon_{xy} = 85$ meV unchanged. We compare in Fig. 11 the experimental Fermi surface (dashed lines) to the one of $\hat{H}^{\mathrm{DFT}} + \hat{H}^{\mathrm{SOC}}_{\lambda_{\mathrm{DFT}}}$. The Fermi surfaces for additionally introduced crystal-field splittings $\Delta\epsilon_{\mathrm{cf}}$ between -80 and 80 meV are shown with solid lines in different shades of red. In contrast to the Fermi surface without SOC ($\lambda = 0$ meV, top-left panel), the Fermi surfaces with the DFT SOC of $\lambda = 100$ meV (top-right panel) resemble the

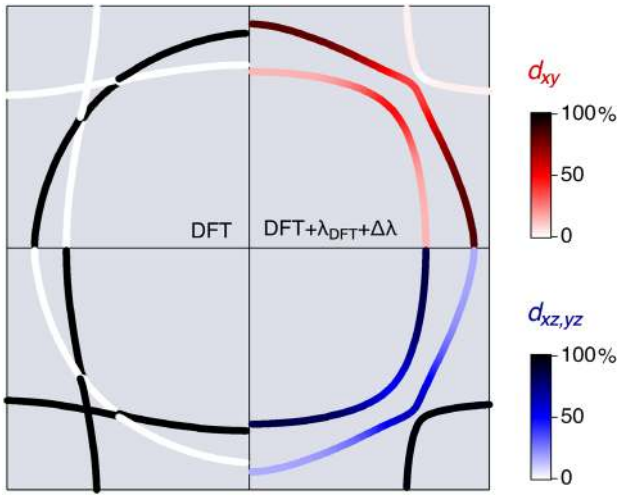

FIG. 10. Orbital character of the DFT FS without SOC at $k_z = 0.4\pi/c$ (left). The orbital character of the DFT + λ_{DFT} + $\Delta\lambda$ eigenstates at the same k_z is reproduced on the right from Fig. 3(g).

overall structure of the experimental Fermi surface. However, the areas of the α and β sheets are too large, and the γ sheet is too small. Importantly, the agreement cannot be improved by adding $\Delta\epsilon_{\mathrm{cf}}$. For example, along ΓM, a $\Delta\epsilon_{\mathrm{cf}}$ of +40 meV would move the Fermi surface closer to the experiment; on the other hand, along ΓX, a $\Delta\epsilon_{\mathrm{cf}}$ of −80 meV would provide the best agreement. The situation is different if we consider an enhanced SOC of $\lambda = 200$ meV (bottom-right panel). Then, we find a nearly perfect agreement with experiment without any additional crystal-field splitting ($\Delta\epsilon_{\mathrm{cf}} = 0$ meV). At an even higher SOC of $\lambda = 300$ meV (bottom-left panel), we see again major discrepancies but with an opposite trend: The α and β sheets are now too small, and the γ sheet is too large. Like in the case of $\lambda = 100$ meV, this cannot be cured by an adjustment of ϵ_{cf}.

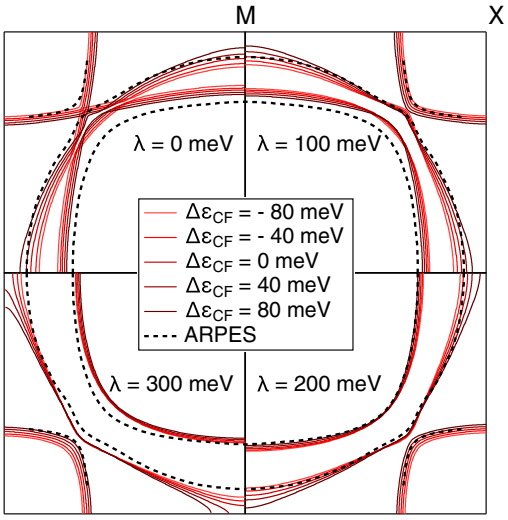

FIG. 11. Fermi surface of Sr_2RuO_4 for $\lambda = 0$ meV (top left), $\lambda = 100$ meV (top right), $\lambda = 200$ meV (bottom right), and $\lambda = 300$ meV (bottom left) compared to ARPES (dashed black line). Note that $\lambda = 100$ meV corresponds to a DFT + SOC calculation and $\lambda = 200$ meV to an effective SOC enhanced by electronic correlations (see main text). The different shades of red indicate additional crystal-field splittings $\Delta\epsilon_{\mathrm{cf}}$ added to $\epsilon_{\mathrm{cf}} = 85$ meV of $\hat{H}^{\mathrm{DFT}}$.

2. DMFT

We perform single-site DMFT calculation with the TRIQS/DFTTools [97] package for $\hat{H}^{\mathrm{DFT}}$ and Hubbard-Kanamori interactions with a screened Coulomb repulsion $U = 2.3$ eV and a Hund's coupling $J = 0.4$ eV based on previous works [20,23]. The impurity problem is solved on the imaginary-time axis with the TRIQS/CTHYB [98] solver at a temperature of 29 K. The employed open-source software tools are based on the TRIQS library [99]. We assume an orbital-independent double counting, and hence it can be absorbed into an effective chemical potential, which is adjusted such that the filling is equal to four electrons. For the analytic continuation of the self-energy to the real-frequency axis, we employ three different methods: Padé approximants (using TRIQS [99]), stochastic continuation (after Beach [100]), and maximum entropy (using TRIQS/maxent [101]). In the relevant energy range from −100 to 0 meV, the difference in the resulting self-energies (Fig. 12) is below the experimental uncertainty. The averaged quasiparticle renormalizations (of the three continuations) are $Z_{xy} = 0.18 \pm 0.01$ and $Z_{xz} = Z_{yz} = 0.30 \pm 0.01$. For all other results presented in the main text, the Padé solution has been used.

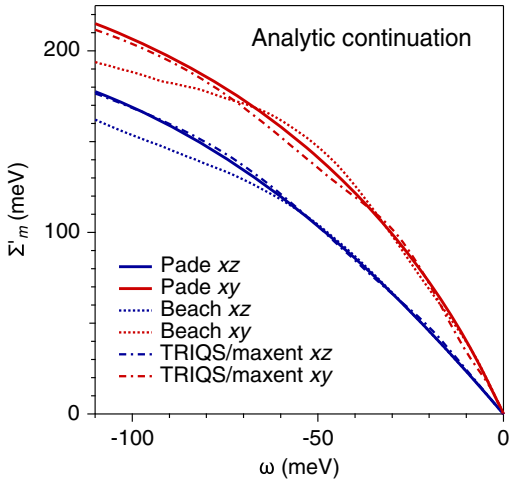

FIG. 12. The real part of DFT + DMFT self-energy in the considered energy range obtained with three different analytic continuation methods: Padé approximants (using TRIQS [99]), stochastic continuation (after Beach [100]), and maximum entropy (using TRIQS/maxent [101]). The difference between the analytic continuation methods is smaller than the experimental error.

Our calculations at a temperature of 29 K use $\hat{H}^{\mathrm{DFT}}$, as the sign problem prohibits reaching such low temperatures with SOC included. Nevertheless, calculations with SOC were successfully carried out at a temperature of 290 K using CT-INT [21] and at 230 K using CT-HYB with a simplified two-dimensional tight-binding model [23]. These works pointed out that electronic correlations in Sr_2RuO_4 lead to an enhanced SOC. To be more precise, Kim *et al.* [23] observed that electronic correlations in this material are described by a self-energy with diagonal elements close to the ones without SOC plus, to a good approximation, frequency-independent off-diagonal elements, which can be absorbed in a static effective SOC strength of $\lambda^{\mathrm{eff}} = \lambda_{\mathrm{DFT}} + \Delta\lambda \simeq 200$ meV—this is the approach followed in the present article.

In addition to the enhancement of SOC, it was observed that low-energy many-body effects also lead to an enhancement of the crystal-field splitting [21,23]. In our DFT + DMFT calculation without SOC, this results in a orbital-dependent splitting in the real part of the self-energies ($\Delta\epsilon_{\mathrm{cf}} = 60$ meV), which would move the γ sheet closer to the van Hove singularity and consequently worsen the agreement with the experimental Fermi surface along the ΓM direction (see bottom-right panel of Fig. 11). Different roots of this small discrepancy are possible, ranging from orbital-dependent double-counting corrections to, in general, DFT being not perfect as "noninteracting" reference point for DMFT. Zhang *et al.* [21] showed that by considering the anisotropy of the Coulomb tensor, the additional crystal-field splitting is suppressed, and consequently, the disagreement between theory and experiment can be cured. We point out that in comparison to the present work, a large enhancement of the crystal-field splitting was observed in Ref. [21], presumably due to the larger interactions employed.

Based on these considerations, we calculate the correlated spectral function $A(\omega, \boldsymbol{k})$ [shown in Fig. 5 of the main text] using the Hamiltonian with enhanced SOC ($\hat{H}^{\mathrm{DFT}} + \hat{H}^{\mathrm{SOC}}_{\lambda_{\mathrm{DFT}}+\Delta\lambda}$) in combination with the frequency-dependent part of the non-SOC (diagonal) self-energy, but we neglect the additional static part introduced by DMFT.

APPENDIX C: OFF-DIAGONAL ELEMENTS OF $\Sigma'_{\nu\nu'}$

In Sec. V A, we extracted $\Sigma'_{\nu\nu}$ under the assumption that the off-diagonal elements can be neglected. To obtain insights about the size of the off-diagonal elements, we use Eq. (12) to calculate the full matrix $\Sigma'_{\nu\nu'}(\omega, \boldsymbol{k})$ in the band basis from the DMFT self-energy in the orbital basis $\Sigma'_m(\omega)$, as shown in Fig. 6(a). This procedure allows us to obtain the full self-energy matrix $\Sigma'_{\nu\nu'}(\omega, \boldsymbol{k})$ at one specific combination of $\boldsymbol{k}$ and ω. Note that for the results presented in Figs. 4 and 13(b), this is not the case because the extracted self-energies for each band correspond to different $\boldsymbol{k}^{\nu}_{\mathrm{max}}$, which are further defined by the experimental MDCs.

In Fig. 13(a), we show the result for two selected $\boldsymbol{k}$ points: on the β sheet for $\theta = 0$ and on the γ sheet for $\theta = 45°$. For these $\boldsymbol{k}$ points, the largest off-diagonal element is $\Sigma'_{\gamma\beta}$, which is about 10%–20% of the size of the diagonal elements. A scan performed for the whole $k_z = 0.4\pi/c$ plane further confirms that $|\Sigma'_{\nu\neq\nu'}|$ is smaller than 20 meV.

However, when neglecting the off-diagonal elements, it is also important to have a large enough energy separation of the bands. This can be understood by considering a simplified case of two bands (ν, ν') and rewriting Eq. (3), which determines the quasiparticle dispersion $\omega^{\mathrm{QP}}_{\nu}(\boldsymbol{k})$, as

$$\omega - \varepsilon_{\nu}(\boldsymbol{k}) - \Sigma'_{\nu\nu}(\omega, \boldsymbol{k}) - \frac{\Sigma'_{\nu\nu'}(\omega, \boldsymbol{k})\Sigma'_{\nu'\nu}(\omega, \boldsymbol{k})}{\omega - \varepsilon_{\nu'}(\boldsymbol{k}) - \Sigma'_{\nu'\nu'}(\omega, \boldsymbol{k})} = 0. \tag{C1}$$

Setting the last term to zero, i.e., using the procedure described in Sec. V A to extract $\Sigma'_{\nu\nu}$, is justified at $\omega = \omega^{\mathrm{QP}}_{\nu}(\boldsymbol{k})$ as long as

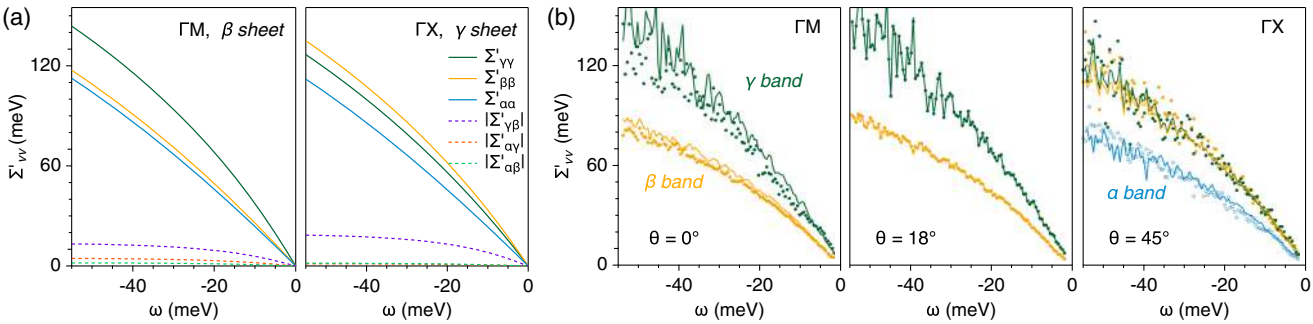

FIG. 13. Reconstructed self-energies in the quasiparticle basis. (a) Full matrix $\Sigma'_{\nu\nu'}(\omega, \boldsymbol{k})$ calculated with Eq. (12) using the DMFT self-energy (shown in Fig. 6(a)) at two selected $\boldsymbol{k}$ points: on the β sheet for $\theta = 0°$ (left) and on the γ sheet for $\theta = 45°$ (right). (b) Directly extracted $\Sigma'_{\nu\nu}(\omega, \boldsymbol{k}^{\nu}_{\mathrm{max}}\,\omega)$ (solid symbols) (Sec. V A) compared to the $\Sigma'_m(\omega, \theta = 18°)$ (Sec. V B) transformed to $\Sigma'_{\nu\nu}(\omega, \boldsymbol{k}^{\nu}_{\mathrm{max}}\,\omega)$ at 0, 18, and 45° (thin lines).

$$\Sigma'_{\nu\nu}(\omega,\boldsymbol{k}) \gg \frac{\Sigma'_{\nu\nu'}(\omega,\boldsymbol{k})\Sigma'_{\nu'\nu}(\omega,\boldsymbol{k})}{\omega-\varepsilon_{\nu'}(\boldsymbol{k})-\Sigma'_{\nu'\nu'}(\omega,\boldsymbol{k})}. \tag{C2}$$

In this condition, the already-small off-diagonal elements enter quadratically. However, in addition, the denominator is not a small quantity because the energy separation of the bare bands $[\varepsilon_\nu(\boldsymbol{k})-\varepsilon_{\nu'}(\boldsymbol{k})]$ is larger than the difference of the diagonal self-energies.

By using the generalized version of Eq. (C2) for all three bands, we find that the right-hand side of this equation is indeed less than 1.2% of $\Sigma'_{\nu\nu}(\omega,\boldsymbol{k}^\nu_{\max}(\omega))$ for all experimentally determined $\boldsymbol{k}^\nu_{\max}(\omega)$. This means that for Sr_2RuO_4, treating each band separately when extracting $\Sigma'_{\nu\nu}$ is well justified in the investigated energy range.

APPENDIX D: RECONSTRUCTION OF $\Sigma'_{\nu\nu}$

In order to further test the validity of the local ansatz [Eq. (12)] and establish the overall consistency of the two procedures used to extract the self-energy in Sec. V, we perform the following "reconstruction procedure." We use the $\Sigma'_m(\omega,\theta_{\boldsymbol{k}})$ (from Sec. V B) at one angle, e.g., $\theta = 18°$, and transform it into $\Sigma'_{\nu\nu}(\omega,\boldsymbol{k}^\nu_{\max}(\omega))$ for other measured angles, using Eq. (12). The good agreement between the self-energy reconstructed in this manner [thin lines in Fig. 13(b)] and its direct determination following the procedure of Sec. V A (dots) confirms the validity of the approximations used throughout Sec. V. It also shows that the origin of the strong momentum dependence of $\Sigma'_{\nu\nu}$ is almost entirely due to the momentum dependence of the orbital content of quasiparticle states, i.e., of $U_{m\nu}(\boldsymbol{k}) = \langle\chi_m(\boldsymbol{k})|\psi_\nu(\boldsymbol{k})\rangle$. In Sr_2RuO_4, the momentum dependence of these matrix elements is mainly due to the SOC.

[1] Y. Maeno, H. Hashimoto, K. Yoshida, S. Nishizaki, T. Fujita, J. G. Bednorz, and F. Lichtenberg, *Superconductivity in a Layered Perovskite without Copper*, Nature (London) **372**, 532 (1994).

[2] T. M. Rice and M. Sigrist, Sr_2RuO_4*: An Electronic Analogue of* ^{3}He*?*, J. Phys. Condens. Matter **7**, L643 (1995).

[3] A. P. Mackenzie and Y. Maeno, *The Superconductivity of* Sr_2RuO_4 *and the Physics of Spin-Triplet Pairing*, Rev. Mod. Phys. **75**, 657 (2003).

[4] A. P. Mackenzie, T. Scaffidi, C. W. Hicks, and Y. Maeno, *Even Odder after Twenty-Three Years: The Superconducting Order Parameter Puzzle of* Sr_2RuO_4, npj Quantum Mater. **2**, 40 (2017).

[5] K. Ishida, H. Mukuda, Y. Kitaoka, K. Asayama, Z. Q. Mao, Y. Mori, and Y. Maeno, *Spin-Triplet Superconductivity in* Sr_2RuO_4 *Identified by* ^{17}O *Knight Shift*, Nature (London) **396**, 658 (1998).

[6] M. S. Anwar, S. R. Lee, R. Ishiguro, Y. Sugimoto, Y. Tano, S. J. Kang, Y. J. Shin, S. Yonezawa, D. Manske, H. Takayanagi, T. W. Noh, and Y. Maeno, *Direct Penetration of Spin-Triplet Superconductivity into a Ferromagnet in* $Au/SrRuO_3/Sr_2RuO_4$ *Junctions*, Nat. Commun. **7**, 13220 (2016).

[7] C. W. Hicks, D. O. Brodsky, E. A. Yelland, A. S. Gibbs, J. A. N. Bruin, M. E. Barber, S. D. Edkins, K. Nishimura, S. Yonezawa, Y. Maeno, and A. P. Mackenzie, *Strong Increase of* T_c *of* Sr_2RuO_4 *under Both Tensile and Compressive Strain*, Science **344**, 283 (2014).

[8] T. Scaffidi, J. C. Romers, and S. H. Simon, *Pairing Symmetry and Dominant Band in* Sr_2RuO_4, Phys. Rev. B **89**, 220510(R) (2014).

[9] J. R. Kirtley, C. Kallin, C. W. Hicks, E.-A. Kim, Y. Liu, K. A. Moler, Y. Maeno, and K. D. Nelson, *Upper Limit on Spontaneous Supercurrents in* Sr_2RuO_4, Phys. Rev. B **76**, 014526 (2007).

[10] A. P. Mackenzie, S. R. Julian, A. J. Diver, G. G. Lonzarich, N. E. Hussey, Y. Maeno, S. Nishizaki, and T. Fujita, *Calculation of Thermodynamic and Transport Properties of* Sr_2RuO_4 *at Low Temperatures Using Known Fermi Surface Parameters*, Phys. C **263**, 510 (1996).

[11] Y. Maeno, K. Yoshida, H. Hashimoto, S. Nishizaki, S.-I. Ikeda, M. Nohara, T. Fujita, A. P. Mackenzie, N. E. Hussey, J. G. Bednorz, and F. Lichtenberg, *Two-Dimensional Fermi Liquid Behavior of the Superconductor* Sr_2RuO_4, J. Phys. Soc. Japan **66**, 1405 (1997).

[12] C. Bergemann, A. P. Mackenzie, S. R. Julian, D. Forsythe, and E. Ohmichi, *Quasi-Two-Dimensional Fermi Liquid Properties of the Unconventional Superconductor* Sr_2RuO_4, Adv. Phys. **52**, 639 (2003).

[13] D. Stricker, J. Mravlje, C. Berthod, R. Fittipaldi, A. Vecchione, A. Georges, and D. van der Marel, *Optical Response of* Sr_2RuO_4 *Reveals Universal Fermi-Liquid Scaling and Quasiparticles beyond Landau Theory*, Phys. Rev. Lett. **113**, 087404 (2014).

[14] S. Raghu, A. Kapitulnik, and S. A. Kivelson, *Hidden Quasi-One-Dimensional Superconductivity in* Sr_2RuO_4, Phys. Rev. Lett. **105**, 136401 (2010).

[15] J. W. Huo, T. M. Rice, and F. C. Zhang, *Spin Density Wave Fluctuations and p-Wave Pairing in* Sr_2RuO_4, Phys. Rev. Lett. **110**, 167003 (2013).

[16] L. Komendová and A. M. Black-Schaffer, *Odd-Frequency Superconductivity in* Sr_2RuO_4 *Measured by Kerr Rotation*, Phys. Rev. Lett. **119**, 087001 (2017).

[17] A. Steppke, L. Zhao, M. E. Barber, T. Scaffidi, F. Jerzembeck, H. Rosner, A. S. Gibbs, Y. Maeno, S. H. Simon, A. P. Mackenzie, and C. W. Hicks, *Strong Peak in* T_c *of* Sr_2RuO_4 *under Uniaxial Pressure*, Science **355**, eaaf9398 (2017).

[18] A. Georges, L. de' Medici, and J. Mravlje, *Strong Correlations from Hund's Coupling*, Annu. Rev. Condens. Matter Phys. **4**, 137 (2013).

[19] A. Liebsch and A. Lichtenstein, *Photoemission Quasiparticle Spectra of* Sr_2RuO_4, Phys. Rev. Lett. **84**, 1591 (2000).

[20] J. Mravlje, M. Aichhorn, T. Miyake, K. Haule, G. Kotliar, and A. Georges, *Coherence-Incoherence Crossover and the Mass-Renormalization Puzzles in* Sr_2RuO_4, Phys. Rev. Lett. **106**, 096401 (2011).

[21] G. Zhang, E. Gorelov, E. Sarvestani, and E. Pavarini, *Fermi Surface of* Sr_2RuO_4*: Spin-Orbit and Anisotropic*

Coulomb Interaction Effects, Phys. Rev. Lett. **116**, 106402 (2016).

[22] J. Mravlje and A. Georges, *Thermopower and Entropy: Lessons from* Sr_2RuO_4, Phys. Rev. Lett. **117**, 036401 (2016).

[23] M. Kim, J. Mravlje, M. Ferrero, O. Parcollet, and A. Georges, *Spin-Orbit Coupling and Electronic Correlations in* Sr_2RuO_4, Phys. Rev. Lett. **120**, 126401 (2018).

[24] T. Oguchi, *Electronic Band Structure of the Superconductor* Sr_2RuO_4, Phys. Rev. B **51**, 1385 (1995).

[25] A. P. Mackenzie, S. R. Julian, A. J. Diver, G. J. McMullan, M. P. Ray, G. G. Lonzarich, Y. Maeno, S. Nishizaki, and T. Fujita, *Quantum Oscillations in the Layered Perovskite Superconductor* Sr_2RuO_4, Phys. Rev. Lett. **76**, 3786 (1996).

[26] A. P. Mackenzie, S. Ikeda, Y. Maeno, T. Fujita, S. R. Julian, and G. G. Lonzarich, *The Fermi Surface Topography of* Sr_2RuO_4, J. Phys. Soc. Japan **67**, 385 (1998).

[27] C. Bergemann, S. Julian, A. Mackenzie, S. NishiZaki, and Y. Maeno, *Detailed Topography of the Fermi Surface of* Sr_2RuO_4, Phys. Rev. Lett. **84**, 2662 (2000).

[28] A. Damascelli, D. Lu, K. Shen, N. Armitage, F. Ronning, D. Feng, C. Kim, Z.-X. Shen, T. Kimura, Y. Tokura, Z. Mao, and Y. Maeno, *Fermi Surface, Surface States, and Surface Reconstruction in* Sr_2RuO_4, Phys. Rev. Lett. **85**, 5194 (2000).

[29] H. Iwasawa, Y. Aiura, T. Saitoh, I. Hase, S. I. Ikeda, Y. Yoshida, H. Bando, M. Higashiguchi, Y. Miura, X. Y. Cui, K. Shimada, H. Namatame, and M. Taniguchi, *Orbital Selectivity of the Kink in the Dispersion of* Sr_2RuO_4, Phys. Rev. B **72**, 104514 (2005).

[30] N. J. C. Ingle, K. M. Shen, F. Baumberger, W. Meevasana, D. H. Lu, Z. X. Shen, A. Damascelli, S. Nakatsuji, Z. Q. Mao, Y. Maeno, T. Kimura, and Y. Tokura, *Quantitative Analysis of* Sr_2RuO_4 *Angle-Resolved Photoemission Spectra: Many-Body Interactions in a Model Fermi Liquid*, Phys. Rev. B **72**, 205114 (2005).

[31] H. Iwasawa, Y. Yoshida, I. Hase, S. Koikegami, H. Hayashi, J. Jiang, K. Shimada, H. Namatame, M. Taniguchi, and Y. Aiura, *Interplay among Coulomb Interaction, Spin-Orbit Interaction, and Multiple Electron-Boson Interactions in* Sr_2RuO_4, Phys. Rev. Lett. **105**, 226406 (2010).

[32] H. Iwasawa, Y. Yoshida, I. Hase, K. Shimada, H. Namatame, M. Taniguchi, and Y. Aiura, *High-Energy Anomaly in the Band Dispersion of the Ruthenate Superconductor*, Phys. Rev. Lett. **109**, 066404 (2012).

[33] V. B. Zabolotnyy, D. V. Evtushinsky, A. A. Kordyuk, T. K. Kim, E. Carleschi, B. P. Doyle, R. Fittipaldi, M. Cuoco, A. Vecchione, and S. V. Borisenko, *Renormalized Band Structure of* Sr_2RuO_4*: A Quasiparticle Tight-Binding Approach*, J. Electron Spectrosc. Relat. Phenom. **191**, 48 (2013).

[34] B. Burganov, C. Adamo, A. Mulder, M. Uchida, P. D. C. King, J. W. Harter, D. E. Shai, A. S. Gibbs, A. P. Mackenzie, R. Uecker, M. Bruetzam, M. R. Beasley, C. J. Fennie, D. G. Schlom, and K. M. Shen, *Strain Control of Fermiology and Many-Body Interactions in Two-Dimensional Ruthenates*, Phys. Rev. Lett. **116**, 197003 (2016).

[35] L. de' Medici, J. Mravlje, and A. Georges, *Janus-Faced Influence of Hund's Rule Coupling in Strongly Correlated Materials*, Phys. Rev. Lett. **107**, 256401 (2011).

[36] A. W. Tyler, A. P. Mackenzie, S. NishiZaki, and Y. Maeno, *High-Temperature Resistivity of* Sr_2RuO_4*: Bad Metallic Transport in a Good Metal*, Phys. Rev. B **58**, R10107 (1998).

[37] A. Georges, G. Kotliar, W. Krauth, and M. J. Rozenberg, *Dynamical Mean-Field Theory of Strongly Correlated Fermion Systems and the Limit of Infinite Dimensions*, Rev. Mod. Phys. **68**, 13 (1996).

[38] X. Deng, K. Haule, and G. Kotliar, *Transport Properties of Metallic Ruthenates: A* DFT + DMFT *Investigation*, Phys. Rev. Lett. **116**, 256401 (2016).

[39] Y. Sidis, M. Braden, P. Bourges, B. Hennion, S. NishiZaki, Y. Maeno, and Y. Mori, *Evidence for Incommensurate Spin Fluctuations in* Sr_2RuO_4, Phys. Rev. Lett. **83**, 3320 (1999).

[40] P. Steffens, Y. Sidis, J. Kulda, Z. Q. Mao, Y. Maeno, I. I. Mazin, and M. Braden, *Spin Fluctuations in* Sr_2RuO_4 *from Polarized Neutron Scattering: Implications for Superconductivity*, Phys. Rev. Lett. **122**, 047004 (2019).

[41] K. Ishida, H. Mukuda, Y. Minami, Y. Kitaoka, Z. Q. Mao, H. Fukazawa, and Y. Maeno, *Normal-State Spin Dynamics in the Spin-Triplet Superconductor* Sr_2RuO_4, Phys. Rev. B **64**, 100501(R) (2001).

[42] T. Imai, A. W. Hunt, K. R. Thurber, and F. C. Chou, ^{17}O *NMR Evidence for Orbital Dependent Ferromagnetic Correlations in* Sr_2RuO_4, Phys. Rev. Lett. **81**, 3006 (1998).

[43] P. Lou, M.-C. Chang, and W.-C. Wu, *Evidence for the Coupling between γ-Band Carriers and the Incommensurate Spin Fluctuations in* Sr_2RuO_4, Phys. Rev. B **68**, 012506 (2003).

[44] B. Kim, S. Khmelevskyi, I. I. Mazin, D. F. Agterberg, and C. Franchini, *Anisotropy of magnetic interactions and symmetry of the order parameter in unconventional superconductor* Sr_2RuO_4, npj Quantum Mater. **2**, 37 (2017).

[45] D. Vollhardt, *Normal* ^3He*: An Almost Localized Fermi Liquid*, Rev. Mod. Phys. **56**, 99 (1984).

[46] Y. Aiura, Y. Yoshida, I. Hase, S. I. Ikeda, M. Higashiguchi, X. Y. Cui, K. Shimada, H. Namatame, M. Taniguchi, and H. Bando, *Kink in the Dispersion of Layered Strontium Ruthenates*, Phys. Rev. Lett. **93**, 117005 (2004).

[47] C. Kim, C. Kim, W. S. Kyung, S. R. Park, C. S. Leem, D. J. Song, Y. K. Kim, S. K. Choi, W. S. Jung, Y. Y. Koh, H. Y. Choi, Y. Yoshida, R. G. Moore, and Z. X. Shen, *Self-Energy Analysis of Multiple-Bosonic Mode Coupling in* Sr_2RuO_4, J. Phys. Chem. Solids **72**, 556 (2011).

[48] H. Iwasawa, Y. Yoshida, I. Hase, K. Shimada, H. Namatame, M. Taniguchi, and Y. Aiura, *'True' Bosonic Coupling Strength in Strongly Correlated Superconductors*, Sci. Rep. **3**, 1930 (2013).

[49] Z. Wang, D. Walkup, P. Derry, T. Scaffidi, M. Rak, S. Vig, A. Kogar, I. Zeljkovic, A. Husain, L. H. Santos, Y. Wang, A. Damascelli, Y. Maeno, P. Abbamonte, E. Fradkin, and V. Madhavan, *Quasiparticle Interference and Strong Electron-Mode Coupling in the Quasi-One-Dimensional Bands of* Sr_2RuO_4, Nat. Phys. **13**, 799 (2017).

[50] S. Akebi, T. Kondo, M. Nakayama, K. Kuroda, S. Kunisada, H. Taniguchi, Y. Maeno, and S. Shin, *Low-Energy Electron-Mode Couplings in the Surface Bands*

of Sr_2RuO_4 *Revealed by Laser-Based Angle-Resolved Photoemission Spectroscopy*, Phys. Rev. B **99**, 081108 (R) (2019).

[51] G.-Q. Liu, V. N. Antonov, O. Jepsen, and O. K. Andersen, *Coulomb-Enhanced Spin-Orbit Splitting: The Missing Piece in the* Sr_2RhO_4 *Puzzle*, Phys. Rev. Lett. **101**, 026408 (2008).

[52] Yu He, I. M. Vishik, M. Yi, S. Yang, Z. Liu, J. J. Lee, S. Chen, S. N. Rebec, D. Leuenberger, A. Zong, C. M. Jefferson, R. G. Moore, P. S. Kirchmann, A. J. Merriam, and Z.-X. Shen, *Invited Article: High Resolution Angle Resolved Photoemission with Tabletop 11 eV Laser*, Rev. Sci. Instrum. **87**, 011301 (2016).

[53] M. Hoesch, T. K. Kim, P. Dudin, H. Wang, S. Scott, P. Harris, S. Patel, M. Matthews, D. Hawkins, S. G. Alcock, T. Richter, J. J. Mudd, M. Basham, L. Pratt, P. Leicester, E. C. Longhi, A. Tamai, and F. Baumberger, *A Facility for the Analysis of the Electronic Structures of Solids and Their Surfaces by Synchrotron Radiation Photoelectron Spectroscopy*, Rev. Sci. Instrum. **88**, 013106 (2017).

[54] K. M. Shen, A. Damascelli, D. H. Lu, N. P. Armitage, F. Ronning, D. L. Feng, C. Kim, Z. X. Shen, D. J. Singh, I. I. Mazin, S. Nakatsuji, Z. Q. Mao, Y. Maeno, T. Kimura, and Y. Tokura, *Surface Electronic Structure of* Sr_2RuO_4, Phys. Rev. B **64**, 180502(R) (2001).

[55] B. Stöger, M. Hieckel, F. Mittendorfer, Z. Wang, D. Fobes, J. Peng, Z. Mao, M. Schmid, J. Redinger, and U. Diebold, *High Chemical Activity of a Perovskite Surface: Reaction of CO with* $Sr_3Ru_2O_7$, Phys. Rev. Lett. **113**, 116101 (2014).

[56] K. M. Shen, N. Kikugawa, C. Bergemann, L. Balicas, F. Baumberger, W. Meevasana, N. J. C. Ingle, Y. Maeno, Z. X. Shen, and A. P. Mackenzie, *Evolution of the Fermi Surface and Quasiparticle Renormalization through a van Hove Singularity in* $Sr_{2-y}La_yRuO_4$, Phys. Rev. Lett. **99**, 187001 (2007).

[57] We note that radial $\boldsymbol{k}$-space cuts are not exactly perpendicular to the Fermi surface. This can cause the velocities v_F and v_b given here to deviate by up to 10% from the Fermi velocity. However, since we evaluate the experimental and theoretical dispersion along the same $\boldsymbol{k}$-space cut, this effect cancels in Fig. 2(d) and does not affect the self-energy determination in Sec. V.

[58] F. Baumberger, N. J. C. Ingle, W. Meevasana, K. M. Shen, D. H. Lu, R. S. Perry, A. P. Mackenzie, Z. Hussain, D. J. Singh, and Z.-X. Shen, *Fermi Surface and Quasiparticle Excitations of* Sr_2RhO_4, Phys. Rev. Lett. **96**, 246402 (2006).

[59] We attribute the higher Fermi velocities reported in some earlier studies [29,31,32,34] to the lower energy resolution, which causes an extended range near the Fermi level where the dispersion extracted from fits to individual MDCs is artificially enhanced, rendering a precise determination of v_F difficult. The much lower value of v_F^{β} along ΓM reported in Ref. [49] corresponds to the surface β band, as shown in Appendix A.

[60] N. Marzari and D. Vanderbilt, *Maximally Localized Generalized Wannier Functions for Composite Energy Bands*, Phys. Rev. B **56**, 12847 (1997).

[61] I. Souza, N. Marzari, and D. Vanderbilt, *Maximally Localized Wannier Functions for Entangled Energy Bands*, Phys. Rev. B **65**, 035109 (2001).

[62] F. Lechermann, A. Georges, A. Poteryaev, S. Biermann, M. Posternak, A. Yamasaki, and O. K. Andersen, *Dynamical Mean-Field Theory Using Wannier Functions: A Flexible Route to Electronic Structure Calculations of Strongly Correlated Materials*, Phys. Rev. B **74**, 125120 (2006).

[63] By restricting the Hamiltonian to the t_{2g} subspace, we neglect the e_g-t_{2g} coupling terms of $\hat{H}_{\lambda}^{\mathrm{SOC}}$. This approximation is valid as long as the e_g-t_{2g} crystal-field splitting is large in comparison to λ, which is the case for Sr_2RuO_4.

[64] K. K. Ng and M. Sigrist, *The Role of Spin-Orbit Coupling for the Superconducting State in* Sr_2RuO_4, Europhys. Lett. **49**, 473 (2000).

[65] I. Eremin, D. Manske, and K. H. Bennemann, *Electronic Theory for the Normal-State Spin Dynamics in* Sr_2RuO_4*: Anisotropy Due to Spin-Orbit Coupling*, Phys. Rev. B **65**, 220502(R) (2002).

[66] M. Haverkort, I. Elfimov, L. Tjeng, G. Sawatzky, and A. Damascelli, *Strong Spin-Orbit Coupling Effects on the Fermi Surface of* Sr_2RuO_4 *and* Sr_2RhO_4, Phys. Rev. Lett. **101**, 026406 (2008).

[67] C. M. Puetter and H.-Y. Kee, *Identifying Spin-Triplet Pairing in Spin-Orbit Coupled Multi-band Superconductors*, Europhys. Lett. **98**, 27010 (2012).

[68] C. N. Veenstra, Z. H. Zhu, M. Raichle, B. M. Ludbrook, A. Nicolaou, B. Slomski, G. Landolt, S. Kittaka, Y. Maeno, J. H. Dil, I. S. Elfimov, M. W. Haverkort, and A. Damascelli, *Spin-Orbital Entanglement and the Breakdown of Singlets and Triplets in* Sr_2RuO_4 *Revealed by Spin- and Angle-resolved Photoemission Spectroscopy*, Phys. Rev. Lett. **112**, 127002 (2014).

[69] A. I. Poteryaev, J. M. Tomczak, S. Biermann, A. Georges, A. I. Lichtenstein, A. N. Rubtsov, T. Saha-Dasgupta, and O. K. Andersen, *Enhanced Crystal-Field Splitting and Orbital-Selective Coherence Induced by Strong Correlations in* V_2O_3, Phys. Rev. B **76**, 085127 (2007).

[70] S. V. Borisenko, D. V. Evtushinsky, Z.-H. Liu, I. Morozov, R. Kappenberger, S. Wurmehl, B. Büchner, A. N. Yaresko, T. K. Kim, M. Hoesch, T. Wolf, and N. D. Zhigadlo, *Direct Observation of Spin-Orbit Coupling in Iron-Based Superconductors*, Nat. Phys. **12**, 311 (2016).

[71] Reference [72] noted that an enhanced effective SOC also improves the description of de Haas van Alphen data.

[72] E. J. Rozbicki, J. F. Annett, J.-R. Souquet, and A. P. Mackenzie, *Spin-Orbit Coupling and k-dependent Zeeman Splitting in Strontium Ruthenate*, J. Phys. Condens. Matter **23**, 094201 (2011).

[73] Using the free-electron final-state approximation, we obtain $k_z = (2m_e\hbar^{-2}(h\nu + U - \Phi) - k_{\parallel}^2)^{1/2} \approx 0.4(0.12)\pi/c$, assuming an inner potential relative to E_F of $U - \Phi = 8.5(1.0)$ eV.

[74] M. Hengsberger, D. Purdie, P. Segovia, M. Garnier, and Y. Baer, *Photoemission Study of a Strongly Coupled Electron-Phonon System*, Phys. Rev. Lett. **83**, 592 (1999).

[75] A. Lanzara, P. V. Bogdanov, X. J. Zhou, S. A. Kellar, D. L. Feng, E. D. Lu, T. Yoshida, H. Eisaki, A. Fujimori, K. Kishio, J. I. Shimoyama, T. Noda, S. Uchida, Z. Hussain, and Z. X. Shen, *Evidence for Ubiquitous Strong*

Electron-Phonon Coupling in High-Temperature Superconductors, Nature (London) **412**, 510 (2001).

[76] A. Tamai, W. Meevasana, P. D. C. King, C. W. Nicholson, A. de la Torre, E. Rozbicki, and F. Baumberger, *Spin-Orbit Splitting of the Shockley Surface State on Cu(111)*, Phys. Rev. B **87**, 075113 (2013).

[77] K. Byczuk, M. Kollar, K. Held, Y. F. Yang, I. A. Nekrasov, T. Pruschke, and D. Vollhardt, *Kinks in the Dispersion of Strongly Correlated Electrons*, Nat. Phys. **3**, 168 (2007).

[78] C. Raas, P. Grete, and G. S. Uhrig, *Emergent Collective Modes and Kinks in Electronic Dispersions*, Phys. Rev. Lett. **102**, 076406 (2009).

[79] K. Held, R. Peters, and A. Toschi, *Poor Man's Understanding of Kinks Originating from Strong Electronic Correlations*, Phys. Rev. Lett. **110**, 246402 (2013).

[80] X. Deng, J. Mravlje, R. Žitko, M. Ferrero, G. Kotliar, and A. Georges, *How Bad Metals Turn Good: Spectroscopic Signatures of Resilient Quasiparticles*, Phys. Rev. Lett. **110**, 086401 (2013).

[81] R. Žitko, D. Hansen, E. Perepelitsky, J. Mravlje, A. Georges, and B. S. Shastry, *Extremely Correlated Fermi Liquid Theory Meets Dynamical Mean-Field Theory: Analytical Insights into the Doping-Driven Mott Transition*, Phys. Rev. B **88**, 235132 (2013).

[82] M. Braden, W. Reichardt, Y. Sidis, Z. Mao, and Y. Maeno, *Lattice Dynamics and Electron-Phonon Coupling in* Sr_2RuO_4*: Inelastic Neutron Scattering and Shell-Model Calculations*, Phys. Rev. B **76**, 014505 (2007).

[83] K. I. Kugel and D. I. Khomskii, *The Jahn-Teller Effect and Magnetism: Transition Metal Compounds*, Sov. Phys. Usp. **25**, 231 (1982).

[84] Y. Tokura and N. Nagaosa, *Orbital Physics in Transition-Metal Oxides*, Science **288**, 462 (2000).

[85] H. Miao, Z. P. Yin, S. F. Wu, J. M. Li, J. Ma, B.-Q. Lv, X. P. Wang, T. Qian, P. Richard, L.-Y. Xing, X.-C. Wang, C. Q. Jin, K. Haule, G. Kotliar, and H. Ding, *Orbital-Differentiated Coherence-Incoherence Crossover Identified by Photoemission Spectroscopy in LiFeAs*, Phys. Rev. B **94**, 201109(R) (2016).

[86] P. O. Sprau, A. Kostin, A. Kreisel, A. E. Böhmer, V. Taufour, P. C. Canfield, S. Mukherjee, P. J. Hirschfeld, B. M. Andersen, and J. C. S. Davis, *Discovery of Orbital-Selective Cooper Pairing in FeSe*, Science **357**, 75 (2017).

[87] M. Braden, O. Friedt, Y. Sidis, P. Bourges, M. Minakata, and Y. Maeno, *Incommensurate Magnetic Ordering in* $Sr_2Ru_{1-x}Ti_xO_4$, Phys. Rev. Lett. **88**, 197002 (2002).

[88] J. E. Ortmann, J. Y. Liu, J. Hu, M. Zhu, J. Peng, M. Matsuda, X. Ke, and Z. Q. Mao, *Competition between Antiferromagnetism and Ferromagnetism in* Sr_2RuO_4 *Probed by Mn and Co Doping*, Sci. Rep. **3**, 2950 (2013).

[89] S. C. Wang, H. B. Yang, A. K. P. Sekharan, H. Ding, J. R. Engelbrecht, X. Dai, Z. Wang, A. Kaminski, T. Valla, T. Kidd, A. V. Fedorov, and P. D. Johnson, *Quasiparticle Line Shape of* Sr_2RuO_4 *and Its Relation to Anisotropic Transport*, Phys. Rev. Lett. **92**, 137002 (2004).

[90] T. E. Kidd, T. Valla, A. V. Fedorov, P. D. Johnson, R. J. Cava, and M. K. Haas, *Orbital Dependence of the Fermi Liquid State in* Sr_2RuO_4, Phys. Rev. Lett. **94**, 107003 (2005).

[91] T. Kondo, M. Ochi, M. Nakayama, H. Taniguchi, S. Akebi, K. Kuroda, M. Arita, S. Sakai, H. Namatame, M. Taniguchi, Y. Maeno, R. Arita, and S. Shin, *Orbital-Dependent Band Narrowing Revealed in an Extremely Correlated Hund's Metal Emerging on the Topmost Layer of* Sr_2RuO_4, Phys. Rev. Lett. **117**, 247001 (2016).

[92] P. Blaha, K. Schwarz, G. K. H. Madsen, D. Kvasnicka, J. Luitz, R. Laskowski, F. Tran, and L. D. Marks, *WIEN2k, An Augmented Plane Wave+Local Orbitals Program for Calculating Crystal Properties* (Karlheinz Schwarz, Techn. Universität Wien, Austria, 2018).

[93] J. P. Perdew, K. Burke, and M. Ernzerhof, *Generalized Gradient Approximation Made Simple*, Phys. Rev. Lett. **77**, 3865 (1996).

[94] J. Kuneš, R. Arita, P. Wissgott, A. Toschi, H. Ikeda, and K. Held, *Wien2wannier: From Linearized Augmented Plane Waves to Maximally Localized Wannier Functions*, Comput. Phys. Commun. **181**, 1888 (2010).

[95] A. A. Mostofi, J. R. Yates, Y. S. Lee, I. Souza, D. Vanderbilt, and N. Marzari, *Wannier90: A Tool for Obtaining Maximally-Localised Wannier Functions*, Comput. Phys. Commun. **185**, 2309 (2014).

[96] T. Vogt and D. J. Buttrey, *Low-Temperature Structural Behavior of* Sr_2RuO_4, Phys. Rev. B **52**, R9843 (1995).

[97] M. Aichhorn, L. Pourovskii, P. Seth, V. Vildosola, M. Zingl, O. E. Peil, X. Deng, J. Mravlje, G. J. Kraberger, C. Martins, M. Ferrero, and O. Parcollet, *TRIQS/DFTTools: A TRIQS Application for Ab Initio Calculations of Correlated Materials*, Comput. Phys. Commun. **204**, 200 (2016).

[98] P. Seth, I. Krivenko, M. Ferrero, and O. Parcollet, *TRIQS/CTHYB: A Continuous-Time Quantum Monte Carlo Hybridisation Expansion Solver for Quantum Impurity Problems*, Comput. Phys. Commun. **200**, 274 (2016).

[99] O. Parcollet, M. Ferrero, T. Ayral, H. Hafermann, I. Krivenko, L. Messio, and P. Seth, *TRIQS: A Toolbox for Research on Interacting Quantum Systems*, Comput. Phys. Commun. **196**, 398 (2015).

[100] K. S. D. Beach, *Identifying the maximum entropy method as a special limit of stochastic analytic continuation*, arXiv:cond-mat/0403055.

[101] *TRIQS/maxent package*, https://triqs.github.io/maxent.

[102] https://doi.org/10.17630/592cc7e7-85bb-4bdc-a229-2250bfb728c5.